Eidgenössische Technische Hochschule Zürich
Swiss Federal Institute of Technology Zurich

Quantum Device Lab

Master's Thesis

Implementation and characterization of multiplexed readout of superconducting qubits

Ants Remm

Supervisors:
Christian Kraglund Andersen
Johannes Heinsoo

Principal Investigator:
Prof. Dr. Andreas Wallraff

Autumn 2017

Contents

1 Introduction

The cost of computation has been in an exponential fall since the advent of digital computation in the middle of the 20th century, halving roughly every 26 months [1]. The affordability of computational power has in one way or another been instrumental in most recent technological advances, for example in rocket engine design, genome sequencing, and artificial intelligence. There are classes of problems however, that are too complex to solve in any realistic time-scale using a classical computer even when taking into account their exponential growth in processing power. These problems include simulation of quantum chemical processes for drug design and material science, and factoring large numbers for cryptographic applications. There are algorithms for solving these types of problems in feasible time, if one turns away from the classical model of computation to the more powerful quantum computation [2, 3]. In addition, the possibility to use quantum superposition to probe the entire classical state-space at once gives rise to a possible speedup in other problems like unstructured database search [4], machine learning [5] and solving systems of linear equations [6]. In classical computation the state s of the computer is usually represented as a set of classical binary variables called bits $s \in \{0,1\}^n$, where n is the size of the state space and the basic operations on the states, called gates, are transformations of the type $g : \{0,1\}^k \to \{0,1\}^l$. In a quantum computer the state space is replaced with a Hilbert space of quantum bits, or *qubits*, $s \in \{|0\rangle, |1\rangle\}^{\otimes n}$ and the gates are unitary transformations on subspaces of the full Hilbert space.

One of the main challenges in building a quantum computer is to isolate the system used to encode the quantum state from its environment to suppress spontaneous emission and dephasing, while retaining enough control over the quantum state to perform gates and measure the quantum state at will. Different physical systems have been proposed to implement a quantum computer, such as Rydberg atoms flying through a microwave cavity [7], cold ions trapped in an electromagnetic trap [8], nuclei of molecules in liquid or solid state [9, 10], localized electrons in semiconductors [11], individual photons [12], defects in diamond lattice [13], and superconducting electrical circuits [14]. In many of the aforementioned systems high-fidelity control over, and readout of, a single or a few qubits has been experimentally demonstrated, but there are still significant challenges in increasing the system size. Two of the most promising platforms are circuit quantum electrodynamics (QED) and ion trap quantum computing. In circuit QED superconducting transmission line resonators and Josephson junction based artificial atoms are

used to build a quantum information processing device. In ion trap quantum computing the ions are isolated from the environment by trapping them in vacuum using a Paul trap and the electronic and motional degrees of freedom are manipulated by applying laser or microwave pulses. Both of these platforms have demonstrated coherent manipulation of order of tens of qubits on a single device. The work in this master's thesis and in Quantum Device Lab in general was carried out on superconducting circuits.

The problem that qubits inevitably decohere would prohibit one from doing long calculations on a quantum computer. This problem can be circumvented by using fault tolerant quantum computation where a logical qubit is encoded in several physical qubits using a quantum error correcting code. As the number of physical qubits used is increased, the error rate of the logical qubit decreases exponentially [15]. The error correcting codes typically work by repeatedly measuring different parity operators of the physical qubits to check if an error has occurred. To achieve a reduction in the error rate of the logical qubit, a threshold for the error probability between the measurements must be overcome. For a constant error rate, it is therefore advantageous to make the correction cycle as short as possible. In a recent proposal by Versluis *et. al.* [16] of a detailed architecture for fault tolerant computation using surface code [17] the measurement takes 500 ns or 71 % of the total error correction cycle. By reducing the measurement time, the cycle could be made shorter, which in turn would reduce the error probability per cycle.

Another challenge in building a large-scale quantum computer in the circuit QED architecture is the amount of required microwave cabling and classical control electronics. To determine the state of a qubit in the circuit QED architecture, one measures the qubit state dependent transmission or reflection amplitude of a microwave resonator (called readout resonator) dispersively coupled to the qubit [14]. Extending this architecture naively to multiple qubits, one would need an independent input and output line, microwave generator, amplifier and detector for each qubit. A more cost effective way of extending to several qubits is to use *frequency-division multiplexing* (FDM). The idea behind FDM is that a different frequency band is used for each readout resonator, all of which are connected to a common feedline on the superconducting device. This enables the use of only a single broadband microwave generator and detection chain. The number of qubits that can be read out using a single detection line is limited by the ratio of available signal generation and detection bandwidth to the spectral width used for reading out a single qubit.

The topic of this master's thesis is the implementation and characterization of FDM readout, or *multiplexed readout*, using the Zurich Instruments ultra high frequency lock-in (UHFLI)[1] instrument, PycQED Python library for communication with measurement instruments and a new sample design for fast, high-fidelity, low-crosstalk readout. In Chapter 2 theoretical aspects of circuit QED, qubit state measurement by linear detection, multiplexed readout and readout crosstalk are reviewed; in Chapter 3 an overview of the experimental setup used for the experiments is given; in Chapter 4 the multiplexed readout experiments and results are discussed; and finally in Chapter 5 the thesis is concluded with a summary and an outlook. In appendix A an overview of the software used is presented together with comments about existing and added features.

[1] Ultra high frequency (UHF) is the frequency band from 300 MHz to 3 GHz

2 Theory overview

In this chapter I will give an overview of the main theoretical aspects relevant for multiplexed readout. In Section 2.1 I will introduce the circuit QED setting we are working in and some of the components that are often used in superconducting quantum processors. The theory behind qubit state measurement and the relevant noise sources will be discussed in Sections 2.2 and 2.3. Finally, in Section 2.4 I will discuss the implementation of multiplexed readout, explain the different sources for crosstalk and report on the analytical model of the microwave properties of the device we have designed for fast, low crosstalk multiplexed readout.

2.1 Circuit QED

A harmonic oscillator coupled to a two-level system is one of the simplest setups where coherent interactions between individual quantum systems can be observed. The dynamics of this system are governed by the Jaynes-Cummings Hamiltonian [18, p. 302]:

$$\hat{H} = -\frac{\hbar\omega_{\mathrm{Q}}}{2}\hat{\sigma}_z + \hbar\omega_{\mathrm{R}}\hat{a}^\dagger\hat{a} + \hbar g(\hat{a}^\dagger\hat{\sigma} + \hat{a}\hat{\sigma}^\dagger). \tag{2.1}$$

Here $\hbar\omega_{\mathrm{Q}}$ is the qubit transition energy, ω_{R} is the resonator angular frequency, $\hbar g$ is the coupling strength between them, $\hat{\sigma}_z = |g\rangle\langle g| - |e\rangle\langle e|$ is the Pauli z operator, $\hat{\sigma} = |g\rangle\langle e|$, $\hat{a}$ is the annihilation operator of the harmonic oscillator, and $|g\rangle$, $|e\rangle$ are the ground and excited state of the two-level system. The interaction term $\hat{a}^\dagger\hat{\sigma} + \hat{a}\hat{\sigma}^\dagger$ is due to the electric dipole interaction between the qubit and the resonator field and initially also includes terms $\hat{a}^\dagger\hat{\sigma}^\dagger$ and $\hat{a}\hat{\sigma}$, which are dropped in the rotating wave approximation, valid under the assumptions $|\omega_{\mathrm{Q}} - \omega_{\mathrm{R}}|, g \ll \omega_{\mathrm{Q}}, \omega_{\mathrm{R}}$ [19]. In practice, the two-level system will always have some decoherence rate γ and the oscillator will have a decay rate κ at which excitations are lost to the surrounding environment. To observe coherent exchange of excitations between the two subsystems, we need to have $g \gg \gamma, \kappa$, which is called the *strong coupling* regime [18, p. 308].

In circuit QED [14, 20] the qubit-resonator system is typically fabricated out of a thin film of superconductor that is deposited on a dielectric substrate using standard lithographic techniques. The advantage of circuit QED is that all of the parameters in the Hamiltonian (2.1) can be engineered over a wide range of values by changing the dimensions of the corresponding circuit

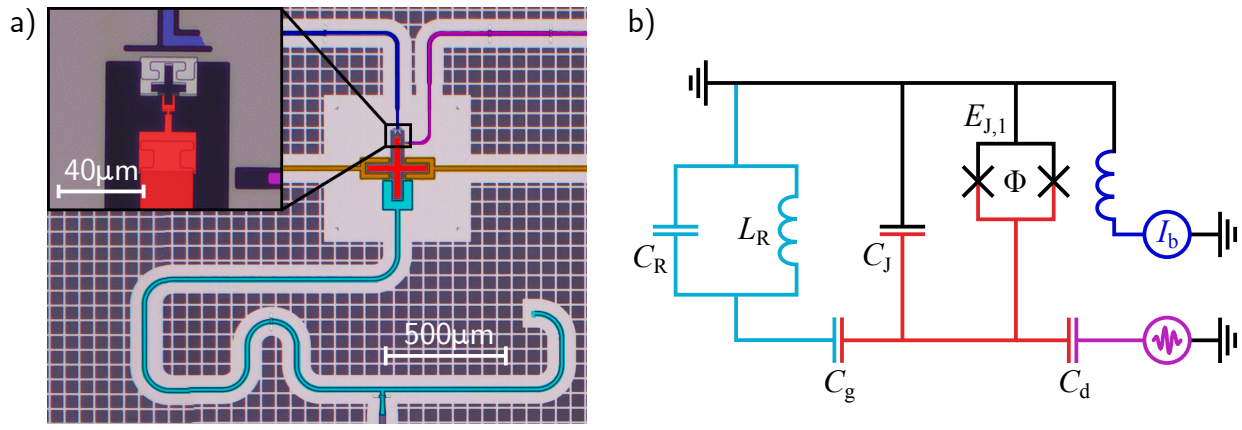

Figure 1: a) A false color micrograph of a charge qubit coupled to a coplanar waveguide resonator. The center conductor of the resonator (cyan) is capacitively coupled to the superconducting island (red). The SQUID loop connecting the island to the ground plane is shown in the inset. The magnetic flux through the SQUID loop can be controlled with the current through the fluxline (blue). The drive line (purple) is used for applying microwave pulses to the qubit to do single qubit rotations. The coupling resonators (orange) couple the qubit to its nearest neighbours. b) An equivalent circuit diagram for the circuit in a) with matching colors. The ground plane is depicted in black. For simplicity the coupling resonators have been left out. C_{R} and L_{R} are the total capacitance and inductance of the resonator, C_{g} and C_{d} are the capacitances of the superconducting island to the inner conductors of the resonator and the drive line, C_{J} is the total capacitance of the center island to the ground, $E_{\mathrm{J},1}$ is the Josephson energy of a single Josephson junction, Φ is the total magnetic flux through the SQUID loop due to the current I_{b}.

elements. A standard way to implement the harmonic oscillator in circuit QED, also used for the samples in this thesis, is to use a coplanar waveguide resonator, the frequency of which can be tuned by changing its length. To isolate a two-level system in the energy spectrum, a nonuniform energy-level spacing is required. This can be achieved by using a Josephson junction which acts as a dissipationless nonlinear inductor. More specifically, we use the *charge qubit* [21] configuration to achieve this. The electrical diagram together with photos of a charge qubit coupled to coplanar waveguide resonator can be seen in Fig. 1.

The Hamiltonian governing the dynamics of the charge qubit is given by [14]

$$\hat{H} = \sum_{N=-\infty}^{\infty} \left[4E_{\mathrm{C}}(N - N_{\mathrm{g}})^2 \left|N\right\rangle\!\left\langle N\right| - E_{\mathrm{J},1} \left| \cos\left(\pi \frac{\Phi}{\Phi_0} \right) \right| \left(\left|N\right\rangle\!\left\langle N+1\right| + \left|N+1\right\rangle\!\left\langle N\right| \right) \right]. \tag{2.2}$$

The charging energy $E_{\mathrm{C}} = \frac{e^2}{2(C_{\mathrm{g}}+C_{\mathrm{d}}+C_{\mathrm{J}})}$ is the energy scale related to adding electrons to the island, $2N_{\mathrm{g}}$ is the number of offset electrons on the island due to a dc bias voltage, $E_{\mathrm{J}} = 2E_{\mathrm{J},1} \left| \cos\left(\pi \frac{\Phi}{\Phi_0} \right) \right|$ is the effective Josephson energy of the superconducting quantum interference device (SQUID) and $\Phi_0 = \frac{h}{2e}$ is the magnetic flux quantum. See also Fig. 1 for circuit parameters. In the regime $E_{\mathrm{J}} \lesssim E_{\mathrm{C}}$ the energy eigenstates of Eq. (2.2) are strongly anharmonic, making it easy to address only the lowest energy transition $g \leftrightarrow e$. However the downside of this regime is that the transition energy also strongly depends on the value of N_{g}, which typically has large fluctuations in practical realizations, called *charge noise*, limiting the qubit coherence times. On the other hand a qubit with $E_{\mathrm{J}} \gg E_{\mathrm{C}}$, called *transmon* [22], is insensitive to charge noise, but has a reduced anharmonicity $\hbar\alpha = E_{e\leftrightarrow f} - E_{g\leftrightarrow e} \approx -E_{\mathrm{C}}$, where $|f\rangle$ is the second excited level of the qubit system. In many applications one can restrict the qubit to the g and e state only, with the transition energy between them

$$\hbar\omega_{\mathrm{Q}} \approx \sqrt{8E_{\mathrm{C}}E_{\mathrm{J}}} - E_{\mathrm{C}} = 4\sqrt{E_{\mathrm{C}}E_{\mathrm{J},1} \left| \cos\left(\pi \frac{\Phi}{\Phi_0} \right) \right|} - E_{\mathrm{C}}, \tag{2.3}$$

effectively recovering the Jaynes-Cummings Hamiltonian (2.1) when coupled to a resonator.

To control the state of the qubit, microwave pulses can be applied to the drive line (see Fig. 1). Let us consider the effect of a pulse with amplitude proportional to $\mathrm{Re}\{\Omega(t)e^{-i\omega_{\mathrm{d}}t}\}$, where ω_{d} is the carrier frequency and $\Omega(t)$ the complex envelope of the pulse. The corresponding interaction Hamiltonian in the rotating wave approximation, restricted to the $\{|g\rangle, |e\rangle\}$ subspace of the qubit is

$$\hat{H}_{\mathrm{d}} = \hbar\Omega(t)e^{-i\omega_{\mathrm{d}}t}\hat{\sigma}^\dagger + \hbar\Omega(t)^* e^{i\omega_{\mathrm{d}}t}\hat{\sigma}. \tag{2.4}$$

By choosing appropriate phase, length and amplitude of the pulse, arbitrary rotations of the qubit state around an axis parallel to the x-y plane on the Bloch sphere can be made. In case the drive pulse has spectral components overlapping the $e \leftrightarrow f$ transition frequency, the $|f\rangle$ and state will also become populated resulting in leakage out of the $|g\rangle$, $|e\rangle$ basis (computational basis). This sets a lower bound on the length the pulse if special care is not taken to avoid exciting the higher energy levels of the qubit system [22].

To extract any information from a quantum computer, it is necessary to measure the qubit's state. To be able to reuse the qubit quickly after the measurement, it is desirable that the qubit is left in a known state. If after the measurement the system's state is equal to the measurement result, the measurement is called *quantum non-demolition* (QND) [23]. This is achieved when the measured observable $\hat{O}$ commutes with the system Hamiltonian $\hat{H}_{\text{sys.}}$. QND measurements are achieved in circuit QED by measuring the qubit state dependent transmission of a coupled resonator, called *readout resonator*, with the qubit-resonator detuning large compared to the coupling $\Delta \equiv \omega_{\text{Q}} - \omega_{\text{R}} \gg g$. This regime of the qubit-resonator system is also called the *dispersive regime*. Expanding the full Hamiltonian of a transmon qubit coupled to a resonator in the powers of the small parameters g_i/Δ_i, where g_i is the coupling rate of the i'th transition of the transmon to the resonator ($g_0 \equiv g$) and Δ_i the transition's detuning from the resonator frequency ($\Delta_0 \equiv \Delta$), and keeping only terms up to second power in g_i/Δ_i, we are left with the dispersive Hamiltonian

$$\hat{H} = -\frac{\hbar\omega'_{\text{Q}}}{2}\hat{\sigma}_z + (\hbar\omega'_{\text{R}} - \hbar\chi\hat{\sigma}_z)\hat{a}^\dagger\hat{a}. \tag{2.5}$$

The qubit and resonator frequencies get renormalized due to interactions with higher energy levels of the transmon, $\omega'_{\text{Q}} \approx \omega_{\text{Q}} + g^2/\Delta$ and $\omega'_{\text{R}} \approx \omega_{\text{R}} - g_1^2/2\Delta_1$ [22]. The form of the dispersive Hamiltonian (2.5) is however the same as we would get from the Jaynes-Cummings Hamiltonian in the dispersive limit. From the resonator's perspective the *dispersive coupling* $\chi \approx g^2\alpha/\Delta(\Delta+\alpha)$ is the magnitude of the shift of resonator frequency depending on the qubit state, but it can also be seen as a shift of the qubit frequency depending on the number of photons in the resonator, called *ac-Stark shift* [20, 22, 24]. In the following chapters we will denote the renormalized frequencies as $\omega_{\text{Q}}, \omega_{\text{R}}$ and keep in mind that they are different from the uncoupled values. Driving the resonator with a coherent field, the phase and amplitude of the emitted field become entangled with the state of the qubit and amplification of the emitted field makes the qubit collapse into one of the two states. With the interaction term $\hat{H}_{\text{int.}} = -\hbar\chi\hat{\sigma}_z\hat{a}^\dagger\hat{a}$ we measure the $\hat{O} = \hat{\sigma}_z$ observable of the system $\hat{H}_{\text{sys}} = -\frac{\hbar\omega'_{\text{Q}}}{2}\hat{\sigma}_z$. As the measured observable commutes with the qubit Hamiltonian, the measurement is QND and the qubit remains in the measured state. The dispersive approximation breaks down, however, if the number of photons in the resonator is in the order of the critical photon number $n_{\text{crit.}} = \Delta^2/4g^2$ [14]. In this case terms that do not commute with the $\hat{\sigma}_z$ operator become relevant and changes of the qubit state might occur, breaking the QND-ness of the measurement.

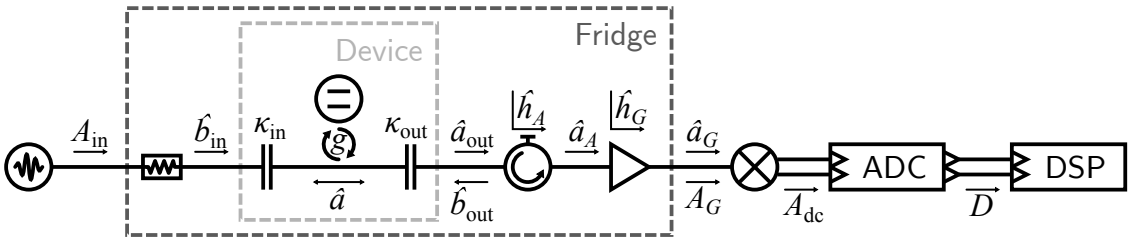

Figure 2: A simplified schematic of the typical elements in a measurement chain. The notation and direction of the signals at different stages of the measurement chain is depicted above or below the signal line. Bosonic quantum signals are depicted as small Latin letters $\hat{a}$ and $\hat{b}$, classical analog signals are denoted with A and digital signals are denoted with D. See text for the description of the linear measurement process.

2.2 Qubit readout by linear detection

In this section we will look quantitatively at how the the qubit state is determined in a dispersive readout scheme. We derive expressions for the signal and the noise of the measurement result by the example of a simple device where a readout resonator coupled to a single qubit is measured in transmission.

The measurement chain relevant for the discussion in this section is depicted in Fig. 2. First a readout pulse is generated at room temperature. In this thesis we only use pulses with a constant amplitude oscillating at a frequency ω_{RO} in the range 6–7.5 GHz. The pulse then enters a dilution refrigerator, where it is attenuated at different temperature stages, so that the thermal noise at room temperature is reduced to negligible levels at the base plate, which is at $\sim$10 mK. The signal is then transmitted through the resonator coupled to the qubit, termed *readout resonator*. The emitted signal passes through an isolator that stops counter-propagating fields from reaching the sample, and is then amplified by a chain of amplifiers at different temperatures. The amplified signal is downconverted to the *intermediate frequency* (IF) ω_{IF}, using an IQ-mixer in our case, and then digitized. The digital signal processing can be done in real time on special purpose signal processing hardware or, if the full timetraces are saved, on a personal computer.

The dynamics of the resonator and the output field are modelled using the input-output formalism [25]. In the Heisenberg picture, the equation of motion for the resonator annihilation

operator $\hat{a}(t)$ is [26, p. 132]

$$\dot{\hat{a}}(t) = -i(\omega_{\mathrm{R}} - \chi\hat{\sigma}_z)\hat{a}(t) - \frac{\kappa_{\mathrm{in}} + \kappa_{\mathrm{out}}}{2}\hat{a}(t) - \sqrt{\kappa_{\mathrm{in}}}\hat{b}_{\mathrm{in}}(t) - \sqrt{\kappa_{\mathrm{out}}}\hat{b}_{\mathrm{out}}(t), \tag{2.6}$$

where $\hat{b}_{\mathrm{in(out)}}(t)$ are the incident fields at the input (output) capacitor with decay rate $\kappa_{\mathrm{in(out)}}$. We assume that $\hat{b}_{\mathrm{out}}(t)$ is in the vacuum state. The Pauli $\hat{\sigma}_z$ operator is however stationary $\dot{\hat{\sigma}}_z(t) = 0$ under the assumption that there are no measurement induced transitions or decay events due to coupling to the environment. The outbound field at the output capacitor $\hat{a}_{\mathrm{out}}(t)$ is given by

$$\hat{a}_{\mathrm{out}}(t) = \sqrt{\kappa_{\mathrm{out}}}\hat{a}(t) + \hat{b}_{\mathrm{out}}(t). \tag{2.7}$$

Because the measurement is QND, we assume the qubit to be in one of the $\hat{\sigma}_z$ eigenstates in the following. In the end, because the entire measurement process is linear, the probability of finding the qubit in either of the eigenstates as a result of the measurement is proportional to the corresponding diagonal element in the density matrix. Therefore we can assume the Pauli z-operator to be a classical variable $\sigma_z \in \{1, -1\}$. To find the output field in terms of the input field and the qubit state, we take a Fourier transform of Eqs. (2.6) and (2.7), and get the relations

$$\hat{a}_{\mathrm{out}}(\omega) = S_{21}(\omega)\hat{b}_{\mathrm{in}}(\omega) + S_{22}(\omega)\hat{b}_{\mathrm{out}}(\omega), \tag{2.8}$$

$$S_{21}(\omega) = \frac{2\sqrt{\kappa_{\mathrm{in}}\kappa_{\mathrm{out}}}}{2i(\omega - \omega_{\mathrm{R}} + \chi\sigma_z) - \kappa_{\mathrm{in}} - \kappa_{\mathrm{out}}}, \tag{2.9}$$

$$S_{22}(\omega) = 1 + \frac{2\kappa_{\mathrm{out}}}{2i(\omega - \omega_{\mathrm{R}} + \chi\sigma_z) - \kappa_{\mathrm{in}} - \kappa_{\mathrm{out}}}. \tag{2.10}$$

The Fourier amplitudes are given by $\hat{c}(\omega) = \frac{1}{\sqrt{2\pi}}\int_{-\infty}^{\infty}\hat{c}(t)e^{i\omega t}\mathrm{d}t$ for $\hat{c} = \hat{a}_{\mathrm{out}}, \hat{b}_{\mathrm{in}}, \hat{b}_{\mathrm{out}}$. While Eq. (2.8) is generally valid for all devices with one input and output port, the exact form of the *scattering parameters* S_{21}, S_{22} given by Eqs. (2.9) and (2.10) will depend on the resonator network.

Due to attenuation in the cables and components, the amplitude of the field at the input of the amplifier $\hat{a}_A$ is reduced by $\sqrt{A}$ compared to the output from the cavity $\hat{a}_{\mathrm{out}}$, where A is the total power attenuation. Since the commutation relation $\left[\hat{a}_{\mathrm{out}}(\omega), \hat{a}^{\dagger}_{\mathrm{out}}(\omega')\right] = \delta(\omega - \omega')$ must also hold for the attenuated signal $\hat{a}_A$, a noise operator $\hat{h}_A$, which we assume to be a bosonic mode, needs to be added to the signal [27]

$$\hat{a}_A(\omega) = \sqrt{A}\hat{a}_{\mathrm{out}}(\omega) + \sqrt{1 - A}\hat{h}_A(\omega), \tag{2.11}$$

so that

$$\begin{aligned}\left[\hat{a}_A(\omega), \hat{a}_A^\dagger(\omega')\right] &= \left[\sqrt{A}\hat{a}_{\text{out}}(\omega) + \sqrt{1-A}\hat{h}_A(\omega), \sqrt{A}\hat{a}_{\text{out}}^\dagger(\omega) + \sqrt{1-A}\hat{h}_A^\dagger(\omega)\right] = \\ &= A\left[\hat{a}_{\text{out}}(\omega), \hat{a}_{\text{out}}^\dagger(\omega')\right] + (1-A)\left[\hat{h}_A(\omega), \hat{h}_A^\dagger(\omega')\right] = \delta(\omega-\omega').\end{aligned} \tag{2.12}$$

Ideally the noise mode is in the vacuum state, but more realistically it will be in a thermal state at temperature T, where the expectation values for the amplitude and its modulus squared are [27]

$$\left\langle \hat{h}_A(\omega) \right\rangle = 0, \tag{2.13a}$$

$$\frac{1}{2}\left\langle \hat{h}_A(\omega)\hat{h}_A^\dagger(\omega') + \hat{h}_A^\dagger(\omega')\hat{h}_A(\omega) \right\rangle = \left\langle \hat{h}_A^\dagger(\omega')\hat{h}_A(\omega) \right\rangle + \frac{1}{2}\delta(\omega-\omega') = \left(N_A + \frac{1}{2}\right)\delta(\omega-\omega'). \tag{2.13b}$$

The noise photon number $N_A = \frac{1}{e^{\hbar\omega/k_{\text{B}}T}-1}$ follows the Bose-Einstein distribution. The 1/2 term represents the intrinsic quantum noise due to simultaneous measurement of two uncommuting observables.

Similarly, for the amplifier to amplify both quadratures equally by $\sqrt{G}$, where G is the power gain of the amplifier, a bosonic noise mode $\hat{h}_G^\dagger$ must be added to the signal [27]. Assuming that the different frequency components of the added noise are not correlated, the noise of the amplifier mode can be written in a form similar to the noise of the attenuator mode

$$\frac{1}{2}\left\langle \hat{h}_G(\omega)\hat{h}_G^\dagger(\omega') + \hat{h}_G^\dagger(\omega')\hat{h}_G(\omega) \right\rangle = \left(N_G + \frac{1}{2}\right)\delta(\omega-\omega'), \tag{2.14}$$

where N_G is the noise photon number of the amplifier.

The output signal from the fridge $\hat{a}_G$ is

$$\hat{a}_G(\omega) = \sqrt{G}\hat{a}_A(\omega) + \sqrt{G-1}\hat{h}_G^\dagger(\omega) = \sqrt{AG}\hat{a}_{\text{out}}(\omega) + \sqrt{G(1-A)}\hat{h}_A(\omega) + \sqrt{G-1}\hat{h}_G^\dagger(\omega). \tag{2.15}$$

If the gain is high enough so that the photon flux of the signal $\hat{a}_G^\dagger(t)\hat{a}_G(t)$ is much higher than the sampling rate of the data acquisition device ν_{s}, we can discard any further quantum noise

and consider it a classical signal $a_G(\omega) = \langle \hat{a}_G(\omega) \rangle + \delta a_G(\omega)$ with the expectation values

$$\langle a_G(\omega) \rangle \equiv \langle \hat{a}_G(\omega) \rangle = \sqrt{AG\kappa_{\text{out}}} \langle \hat{a}(\omega) \rangle = \sqrt{AG} S_{21}(\omega) \left\langle \hat{b}_{\text{in}}(\omega) \right\rangle, \tag{2.16a}$$

$$\begin{aligned} \langle \delta a_G(\omega) \delta a_G^*(\omega') \rangle &\equiv \frac{1}{2} \left\langle \delta \hat{a}_G(\omega) \delta \hat{a}_G^\dagger(\omega') + \delta \hat{a}_G^\dagger(\omega') \delta \hat{a}_G(\omega) \right\rangle = \\ &= AG \left\langle \delta \hat{a}_{\text{out}}^\dagger(\omega') \delta \hat{a}_{\text{out}}(\omega) \right\rangle + G(1-A) N_A \delta(\omega - \omega') + \\ &\quad + (G-1) N_G \delta(\omega - \omega') + \left(G - \frac{1}{2} \right) \delta(\omega - \omega'), \end{aligned} \tag{2.16b}$$

$$\langle \delta a_G(\omega) \delta a_G(\omega') \rangle \equiv \frac{1}{2} \langle \delta \hat{a}_G(\omega) \delta \hat{a}_G(\omega') + \delta \hat{a}_G(\omega') \delta \hat{a}_G(\omega) \rangle = 0. \tag{2.16c}$$

I have denoted the fluctuations of the operators $\hat{O} = \hat{a}_G, \hat{a}$ as $\delta \hat{O}(\omega) \equiv \hat{O}(\omega) - \left\langle \hat{O}(\omega) \right\rangle$ and assumed that the noise modes $\hat{h}_G$ and $\hat{h}_A$ are not correlated with each other or the output mode $\hat{a}_{\text{out}}$. The first term in Eq. (2.16b) is caused by the classical noise in the resonator. For a resonator in a coherent state it will be zero, but in a realistic case, where the inputs are in a thermal state, the result will be proportional to the number of thermal photons in the resonator $N_{\text{th.}}$. This is given by the Bose-Einstein distribution $N_{\text{th.}} = 1/(e^{\hbar\omega_{\text{R}}/k_{\text{B}}T} - 1)$ for the resonator at temperature T. The second and third terms are given by the number of noise photons in the attenuator and amplifier modes, and the last term in Eq. (2.16b) is the inherent quantum noise in phase-preserving amplification. In the following we make the assumption that the noise in the output mode $\hat{a}_{\text{out}}$ is uncorrelated at different frequencies, so that we can write Eq. (2.16b) in terms of the noise spectral density $N(\omega)$:

$$\langle \delta a_G(\omega) \delta a_G^*(\omega') \rangle = N(\omega) \delta(\omega - \omega'), \tag{2.17}$$

$$N(\omega) = AGN_{\text{th.}} + G(1-A)N_A + (G-1)N_G + G - \frac{1}{2}, \tag{2.18}$$

Here we have explicitly included the possibility that the noise is frequency dependent.

The signal $a_G(\omega)$ is given in the units of photons per square root hertz. To convert it to a voltage spectral density $A_G(\omega)$, we must multiply it by the spectral density of the voltage vacuum fluctuations $V_0(\omega) = \sqrt{\hbar\omega Z_0/2}$, where Z_0 is the impedance of the transmission line [28]:

$$A_G(\omega) = \begin{cases} V_0(\omega) a_G(\omega) & \text{for } \omega \geq 0, \\ A_G^*(-\omega) & \text{for } \omega < 0, \end{cases} \tag{2.19}$$

The expression for the negative frequencies is due to the voltage being a real quantity. In time domain we get the expression for the signal in volts

$$A_G(t) = \frac{1}{\sqrt{2\pi}} \int_{-\infty}^{\infty} A_G(\omega) e^{-i\omega t} \mathrm{d}\omega = \sqrt{\frac{\hbar Z_0}{4\pi}} \int_0^{\infty} \left(a_G(\omega) e^{-i\omega t} + a_G^*(\omega) e^{i\omega t} \right) \sqrt{\omega} \mathrm{d}\omega. \tag{2.20}$$

The amplified signal is downconverted by multiplying it with a sinusoidal *local oscillator* (LO) signal at frequency ω_{LO} using a microwave mixer. We use an *IQ-mixer*, which has two outputs, one of which has the LO phase shifted 90°. The two outputs of the mixer are

$$A_I(t) = A_G(t) \cos(\omega_{\mathrm{LO}} t), \qquad \text{and} \qquad A_Q(t) = A_G(t) \sin(\omega_{\mathrm{LO}} t), \tag{2.21}$$

By considering the two real signals $A_I(t)$ and $A_Q(t)$ to be the real and imaginary part of a single complex signal $A_{\mathrm{dc}}(t) = A_I(t) + iA_Q(t)$, we can write downconverted signal at the output of the mixer conveniently as $A_{\mathrm{dc}}(t) = A_G(t) e^{i\omega_{\mathrm{LO}} t}$ or in frequency domain

$$A_{\mathrm{dc}}(\omega) = A_G(\omega + \omega_{\mathrm{LO}}) = \begin{cases} V_0(\omega + \omega_{\mathrm{LO}}) a_G(\omega + \omega_{\mathrm{LO}}) & \text{if } \omega \geq -\omega_{\mathrm{LO}}, \\ A_{\mathrm{dc}}^*(-\omega) & \text{otherwise.} \end{cases} \tag{2.22}$$

The mixer also adds noise to the signal [29] which we discard here, as it is typically small compared to the amplified quantum noise in the signal already. A more rigorous condition of when we can ignore the noise at later stages of the measurement chain will be derived in Section 2.3.

The signal then passes through a low-pass filter with a cutoff frequency $\omega_{\mathrm{IF,max}} < \omega_{\mathrm{LO}}$, that filters out all frequencies $|\omega| > \omega_{\mathrm{IF,max}}$. For simplicity, I assume that the filter has an infinitely sharp cutoff, where in practice higher frequencies are only gradually more attenuated. The remaining signal Fourier amplitude is proportional to the amplified photon field a_G, but downconverted from the readout carrier frequency ω_{RO} to the IF $\omega_{\mathrm{IF}} = \omega_{\mathrm{RO}} - \omega_{\mathrm{LO}}$. For $|\omega| \leq \omega_{\mathrm{IF,max}}$ we have

$$A_{\mathrm{dc}}(\omega) = V_0(\omega + \omega_{\mathrm{LO}}) a_G(\omega + \omega_{\mathrm{LO}}). \tag{2.23}$$

Next the two components of this signal are digitized, using an analog-digital converter (ADC) with sampling rate ν_{S}. To avoid aliasing in the digitized signal, the analog low-pass filter cut-off frequency is chosen to be lower than the Nyquist frequency $\omega_{\mathrm{IF,max}} < \pi\nu_{\mathrm{S}}$. The digitized signal

is given by sampling the downconverted signal as given by Eq. (2.23) at discrete time-points $t = k/\nu_{\mathrm{S}}$

$$D[k] \equiv A_{\mathrm{dc}}(k/\nu_{\mathrm{S}}) = \frac{1}{\sqrt{2\pi}} \int_{-\omega_{\mathrm{IF,max}}}^{\omega_{\mathrm{IF,max}}} V_0(\omega + \omega_{\mathrm{LO}}) a_G(\omega + \omega_{\mathrm{LO}}) e^{-i\omega k/\nu_{\mathrm{S}}} \mathrm{d}\omega. \tag{2.24}$$

Under the assumption that the length of the digitized timetrace $k_{\max}$ is long enough to cover the entire pulse, the Fourier transform of the acquired signal can be expressed as

$$\begin{aligned} D(\omega) &\equiv \frac{1}{\sqrt{2\pi\nu_{\mathrm{S}}}} \sum_{k=0}^{k_{\max}-1} D[k] e^{i\omega k/\nu_{\mathrm{S}}} = \frac{1}{\sqrt{2\pi\nu_{\mathrm{S}}}} \sum_{k=-\infty}^{\infty} D[k] e^{i\omega k/\nu_{\mathrm{S}}} = \\ &= \frac{1}{2\pi\sqrt{\nu_{\mathrm{S}}}} \int_{-\omega_{\mathrm{IF,max}}}^{\omega_{\mathrm{IF,max}}} A_{\mathrm{dc}}(\omega') \sum_{k=-\infty}^{\infty} e^{i(\omega-\omega')k/\nu_{\mathrm{S}}} \mathrm{d}\omega' = \\ &= \sqrt{\nu_{\mathrm{S}}} \int_{-\omega_{\mathrm{IF,max}}}^{\omega_{\mathrm{IF,max}}} A_{\mathrm{dc}}(\omega') \sum_{n=-\infty}^{\infty} \delta(\omega - \omega' - 2\pi n\nu_{\mathrm{S}}) \mathrm{d}\omega' = \\ &= \sqrt{\nu_{\mathrm{S}}} A_{\mathrm{dc}}(\omega) = \sqrt{\nu_{\mathrm{S}}} V_0(\omega + \omega_{\mathrm{LO}}) a_G(\omega + \omega_{\mathrm{LO}}). \end{aligned} \tag{2.25}$$

In case that the window of integration is shorter than the duration of the input signal, the spectrum $D(\omega)$ is convolved with a corresponding window function.

To determine the qubit state, the digitized samples $D[k]$ are multiplied with arbitrarily programmable selected integration weights $w[k]$ and summed in the digital signal processor (DSP) to yield the *integrated signal*

$$\mathcal{S} = \mathrm{Re}\left\{ \sum_{k=0}^{k_{\max}-1} w[k] D[k] \right\}. \tag{2.26}$$

In the same formalism the imaginary part of the sum $\sum_{k=0}^{k_{\max}-1} w[k]D[k]$ can be extracted by choosing the $-iw[k]$ as the integration weights.

While integration is done in time-domain in the DSP, it is insightful to also calculate the result in frequency domain. For this we will define the Fourier transform of the integration weights similarly to the Fourier transform of the digitized signal $w(\omega) \equiv \frac{1}{\sqrt{2\pi\nu_{\mathrm{s}}}} \sum_{k=0}^{k_{\max}-1} w[k] e^{i\omega k/\nu_{\mathrm{s}}}$ and $w[k] = \frac{1}{\sqrt{2\pi\nu_{\mathrm{s}}}} \int_{-\pi\nu_{\mathrm{S}}}^{\pi\nu_{\mathrm{S}}} w(\omega) e^{-i\omega k/\nu_{\mathrm{s}}} \mathrm{d}\omega$ to see that the final integration result will be

$$\mathcal{S} = \mathrm{Re}\left\{ \int_{-\pi\nu_{\mathrm{s}}}^{\pi\nu_{\mathrm{s}}} D(\omega) w(-\omega) \mathrm{d}\omega \right\}, \tag{2.27}$$

with mean and variance

$$\langle \mathcal{S} \rangle = \sqrt{AG\nu_{\mathrm{S}}} \int_{\omega_{\mathrm{LO}}-\pi\nu_{\mathrm{s}}}^{\omega_{\mathrm{LO}}+\pi\nu_{\mathrm{s}}} V_0(\omega)\,\mathrm{Re}\Big\{ S_{21}(\omega)\Big\langle \hat{b}_{\mathrm{in}}(\omega)\Big\rangle w(\omega_{\mathrm{LO}}-\omega)\Big\}\mathrm{d}\omega, \tag{2.28a}$$

$$\left\langle \delta\mathcal{S}^2 \right\rangle = \frac{\nu_{\mathrm{s}}}{2} \int_{\omega_{\mathrm{LO}}-\pi\nu_{\mathrm{s}}}^{\omega_{\mathrm{LO}}+\pi\nu_{\mathrm{s}}} V_0(\omega)^2 N(\omega) |w(\omega_{\mathrm{LO}}-\omega)|^2 \mathrm{d}\omega. \tag{2.28b}$$

To exemplify how this integrated signal can be used to determine the qubit state, we look at the case of a long square pulse with length τ as an input $\left\langle \hat{b}_{\mathrm{in}}(t)\right\rangle = b_0 e^{-i\omega_{\mathrm{RO}}t}$ and constant amplitude integration weights oscillating at the IF $\omega_{\mathrm{IF}} = \omega_{\mathrm{RO}} - \omega_{\mathrm{LO}}$, $w[k] = w_0 e^{i\omega_{\mathrm{IF}}k/\nu_{\mathrm{s}}}$, where b_0 and w_0 are the corresponding possibly complex amplitudes. In the steady state limit $\tau \gg \frac{1}{\kappa_{\mathrm{in}}+\kappa_{\mathrm{out}}}$ the bandwidth of $w(\omega)$ and $\left\langle \hat{b}_{\mathrm{in}}(t)\right\rangle$ is small enough that we can consider their product to be proportional to the Dirac delta function $\left\langle \hat{b}_{\mathrm{in}}(\omega)\right\rangle w(\omega_{\mathrm{LO}}-\omega) \approx b_0 w_0 \sqrt{\nu_{\mathrm{S}}}\tau\delta(\omega-\omega_{\mathrm{RO}})$. The signal and noise terms become then

$$\langle \mathcal{S} \rangle = \nu_{\mathrm{S}}\tau\sqrt{AG} V_0(\omega_{\mathrm{RO}})\,\mathrm{Re}\{S_{21}(\omega_{\mathrm{RO}}) b_0 w_0\} \tag{2.29a}$$

$$\left\langle \delta\mathcal{S}^2 \right\rangle = \nu_{\mathrm{s}}^2 \tau V_0(\omega_{\mathrm{RO}})^2 N(\omega_{\mathrm{RO}}) |w_0|^2/2 \tag{2.29b}$$

Because the scattering parameter S_{21} depends on the qubit state, we can deduce the qubit state from the integrated result by choosing the phase of w_0 or b_0 appropriately. A threshold value $\mathcal{S}_{\mathrm{th.}}$ is chosen between the expectation values for $\mathcal{S}$ for the ground and excited states, such that if $\mathcal{S} > \mathcal{S}_{\mathrm{th.}}$ we label the outcome as the qubit being in the corresponding state.

2.3 Measurement efficiency

The goodness of the measurement depends on how well we can determine state of the qubit from a single integration result $\mathcal{S}$. This is characterized by the signal to noise ratio (SNR), defined as

$$\mathrm{SNR} \equiv \frac{\langle \mathcal{S}^e \rangle - \langle \mathcal{S}^g \rangle}{\sqrt{\langle \delta\mathcal{S}^2 \rangle}}, \tag{2.30}$$

where the superscript g (e) denotes the qubit state. For the steady state case 2.29a and (2.29b), the efficiency is given by

$$\mathrm{SNR}^2 = \frac{2\tau AG |b_0|^2 |S_{21}^e(\omega_{\mathrm{RO}}) - S_{21}^g(\omega_{\mathrm{RO}})|^2}{N(\omega_{\mathrm{RO}})}, \tag{2.31}$$

if we choose the optimal integration phase $\arg(w_0) = -\arg(S_{21}(\omega_{\mathrm{RO}})) - \arg(b_0)$. From Eq. (2.31) we see that the SNR can always be increased by increasing the drive amplitude b_0. In practice we are limited by the number of photons in the readout resonator n_{RO} during readout, which should not be much larger than the critical photon number $n_{\mathrm{crit.}}$ for the dispersive approximation to hold. For the steady state the number of photons in the readout resonator is given by

$$n_{\mathrm{RO}} = \lim_{t\to\infty} \left\langle \hat{a}^\dagger(t)\hat{a}(t) \right\rangle = \frac{4\kappa_{\mathrm{in}}|b_0|^2}{4(\omega_{\mathrm{R}} - \chi\sigma_z - \omega_{\mathrm{RO}})^2 + (\kappa_{\mathrm{in}} + \kappa_{\mathrm{out}})^2} = \frac{|S_{21}(\omega_{\mathrm{RO}})|^2}{\kappa_{\mathrm{out}}}|b_0|^2. \tag{2.32}$$

The transmission amplitudes for the qubit in the ground and excited state are in general different, and therefore so are the numbers of readout photons. Because we want to keep the measurement QND for both qubit states, we are interested in the number of readout photons in the readout resonator in the worst of the two cases $n_{\mathrm{RO,max}} = \max(n^g_{\mathrm{RO}}, n^e_{\mathrm{RO}})$. We find an expression for the SNR in terms of $n_{\mathrm{RO,max}}$:

$$\mathrm{SNR}^2 = \tau n_{\mathrm{RO,max}} \frac{\kappa_{\mathrm{out}}|S^e_{21} - S^g_{21}|^2}{\max\left(|S^g_{21}|^2, |S^e_{21}|^2\right)} \frac{AG}{N}. \tag{2.33}$$

The first term $\tau n_{\mathrm{RO,max}}$ describes the duration and strength of the readout. We typically want the readout to be fast for the qubit not to decay during the readout and not too strong so that the dispersive Hamiltonian still holds. These requirements set an upper limit on how big we can make the first term. The second term $\kappa_{\mathrm{out}}|S^e_{21} - S^g_{21}|^2 \Big/ \max\left(|S^g_{21}|^2, |S^e_{21}|^2\right)$ depends on the properties of the device: $\chi, \kappa_{\mathrm{out}}, \omega_{\mathrm{R}}$ and the used readout frequency ω_{RO}. It is maximized for $\omega_{\mathrm{RO}} = \omega_{\mathrm{R}}$ and $\kappa_{\mathrm{out}} = 2|\chi|$. The last term AG/N describes the gain and noise added to the output signal $\hat{a}_{\mathrm{out}}(t)$.

The *measurement efficiency* η is the squared ratio of the achieved SNR to the SNR determined by the quantum noise in the output signal from the device $\hat{a}_{\mathrm{out}}$ only, while keeping the device and readout pulse parameters constant. In the case of a long square readout pulse studied above, it would be given by

$$\eta \equiv \frac{\mathrm{SNR}^2}{\mathrm{SNR}^2_{\mathrm{q.l.}}} = \frac{AG}{N} = \left(\frac{1}{2} + N_{\mathrm{th.}} + \left(1 - A^{-1}\right)\left(N_A + \frac{1}{2}\right) + \frac{(1 - G^{-1})\left(N_G + \frac{1}{2}\right)}{A}\right), \tag{2.34}$$

where the subscript q.l. denotes the quantum limit. So far we have assumed that no additional noise or gain is added after the first first amplifier. In practice there are usually several amplifiers

at different temperatures that add gain and noise to the signal. In this case we can extend Eq. (2.34) according to Friis' equation [30, p. 505]

$$\frac{1}{\eta} = \left(N_{\text{th.}} + \frac{1}{2}\right) + \left(1 - A^{-1}\right)\left(N_A + \frac{1}{2}\right) + \frac{\left(1 - G^{-1}\right)\left(N_G + \frac{1}{2}\right)}{A} + \frac{N_{G_3}}{AG} + \frac{N_{G_4}}{AGG_3} + \ldots \quad (2.35)$$

where the noise terms from later amplifiers N_{G_i} have a progressively smaller effect on the total efficiency as the original signal is amplified by the previous amplifiers with gain G_j. In each term, the numerator is equal to the extra noise added at that amplification stage, and the denominator is the total gain before that stage. Each of the $\frac{1}{2}$ terms correspond to the quantum noise added to the system. In this formalism the attenuator is considered on the same terms as the amplifiers but with a "gain" of $A < 1$. Looking at the structure of Eq. (2.35), 3 criteria necessary for achieving an efficiency close to unity can be formulated: The attenuation before the first amplifier should be as low as possible $1 - A \ll 1$. The first amplifier should work close to the quantum limit, adding as little noise as possible $N_G \ll 1$. And thirdly, the noise from subsequent amplifiers should be small compared to the amplified signal $N_{G_i} / \prod_{j<i} G_j \ll 1$. For example in the setup used in this thesis the first amplifier has $G = 20\,\text{dB}$ of gain and overcomes the noise of the second high-electron-mobility transistor (HEMT) amplifier. The HEMT amplifier is thermalized to the 4 K stage of the cryostat and therefore has a noise temperature of $T_{\text{HEMT}} \approx 4\,\text{K}$.

$$G \approx 20\,\text{dB} = 100 \gg 12 \approx \left(e^{\frac{\hbar\omega_{\text{RO}}}{k_{\text{B}}T_{\text{HEMT}}}} - 1\right)^{-1} = N_{\text{HEMT}} \quad (2.36)$$

Therefore the third criterion is satisfied. We have normalised the measurement efficiency to the maximum achievable SNR with a phase preserving amplifier. Using a phase sensitive amplifier, which uses the same mode that is amplified as the $\hat{h}_G$ mode, no quantum noise is added at the amplification stage and it is possible to achieve measurement efficiencies up to 2 by this definition. Therefore the measurement efficiency is often defined to be 2 times smaller than defined here.

2.3.1 Filter efficiency

In the previous chapter we derived the formula for SNR in the case of a long measurement pulse so that the readout resonator is in the steady state. In many cases we want the readout to be fast and therefore we can not make the steady state assumption. In the general case the achieved SNR depends on the choice of the integration weights and is characterized by the *filter efficiency* η_{f}. Here, we will study this dependence quantitatively.

Expressing Eqs. (2.28a) and (2.28b) in time domain with the assumption of constant noise spectrum $V_0^2(\omega)N(\omega) = V_0^2 N$, we get

$$\langle \mathcal{S} \rangle = \mathrm{Re}\left\{ \sum_{k=0}^{k_{\max}-1} w[k]\langle D[k] \rangle \right\}, \tag{2.37a}$$

$$\left\langle \delta \mathcal{S}^2 \right\rangle = \frac{V_0^2 N \nu_{\mathrm{s}}}{2} \sum_{k=0}^{k_{\max}-1} |w[k]|^2. \tag{2.37b}$$

The signal to noise ratio in this general case is given by

$$\mathrm{SNR}^2 = \frac{2\left(\sum_{k=0}^{k_{\max}-1} \mathrm{Re}\{w[k]\Delta D[k]\}\right)^2}{V_0^2 N \nu_{\mathrm{s}} \sum_{k=0}^{k_{\max}-1} |w[k]|^2}. \tag{2.38}$$

Here we have denoted the difference of average excited and ground state signals as $\Delta D = \langle D^e \rangle - \langle D^g \rangle$. We can look at Eq. (2.38) as a function of the $2k_{\max}$ variables $w[k]$ and $w^*[k]$ and maximize the SNR in terms of them:

$$\frac{\partial \mathrm{SNR}^2}{\partial w[k]} = 0 \qquad \Rightarrow \qquad w^*[k] \propto \Delta D[k]. \tag{2.39}$$

It is therefore optimal to use the complex conjugate of the mean difference of the excited and ground state response of the system as the integration weights. These integration weights are also called a *mode-matched* filter as they match the temporal profile of the input signal mode. This insight allows us to calculate the filter efficiency

$$\eta_{\mathrm{f}} \equiv \frac{\mathrm{SNR}^2}{\mathrm{SNR}^2_{\mathrm{opt}.w}} = \frac{\left(\sum_{k=0}^{k_{\max}-1} \mathrm{Re}\{w[k]\Delta D[k]\}\right)^2}{\sum_{k=0}^{k_{\max}-1} |w[k]|^2 \sum_{k=0}^{k_{\max}-1} |\Delta D[k]|^2}, \tag{2.40}$$

where $\mathrm{SNR}_{\mathrm{opt}.w}$ is the achieved SNR using the optimal weights.

The simplest way to experimentally determine the optimal weight function is to repeatedly prepare the qubit in g and e state and measure the average time-evolution of $D[k]$. Since the acquired samples will include noise, the expected value of the filter efficiency will be a function of the number of averages n_{avg}. Let us denote the experimentally determined integration weights after n_{avg} rounds of averaging as $w_n[k] = \Delta D^*[k] + \delta w_n[k]$. The deviations $\delta w_n[k]$ will have the expectation values

$$\langle \delta w_n[k] \rangle = 0, \qquad \langle \delta w_n[k] \delta w_n[l] \rangle = 0, \qquad \langle \delta w_n[k] \delta w_n^*[l] \rangle = \delta_{kl} 2V_0^2 N \nu_{\mathrm{s}} / n_{\mathrm{avg}}. \tag{2.41}$$

Expanding the expectation value of the filter efficiency after n_{avg} averages, $\langle \eta_{\text{f}}^n \rangle$, as a function of $w[k]$ and $w^*[k]$ in a Taylor series around the optimal value up to quadratic terms, we get

$$\begin{aligned}\langle \eta_{\text{f}}^n \rangle &\approx 1 + \sum_{k=0}^{k_{\max}-1} \left. \frac{\partial^2 \eta_{\text{f}}}{\partial w[k] \partial w^*[k]} \right|_{w[l]=\Delta D^*[l]} \langle \delta w_n[k] \delta w_n^*[k] \rangle = \\ &= 1 - \frac{(2k_{\max}-1)\nu_{\text{s}} V_0^2 N}{n_{\text{avg}} \sum_{k=0}^{k_{\max}-1} |\Delta D[k]|^2} = 1 - \frac{2(2k_{\max}-1)}{n_{\text{avg}} \text{SNR}_{\text{opt}.w}^2} = \frac{1}{1 + \frac{2(2k_{\max}-1)}{n_{\text{avg}} \text{SNR}^2}}.\end{aligned} \tag{2.42}$$

The variation of the expectation value is

$$\left\langle \left(\eta_{\text{f}}^n - \langle \eta_{\text{f}}^n \rangle \right)^2 \right\rangle \approx \left(1 - \langle \eta_{\text{f}}^n \rangle \right)^2. \tag{2.43}$$

As we increase the number of averages n_{avg}, the filter efficiency approaches unity at the scale $\frac{4k_{\max}-2}{\text{SNR}^2}$. The variations in the expected filter efficiency are in the same order as deviations from unity. This gives us a practical way to check if we have taken enough averages for determining the optimal integration weights.

2.3.2 Efficiency loss due to mixer imperfection

Eq. (2.21) describes the operation of an ideal IQ-mixer, but real mixers implement these equations only approximately. Typical imperfections, that IQ-mixers suffer from, are signals at higher harmonic frequencies and phase and amplitude imbalance. Here we will study the effects of the phase imbalance φ and the amplitude imbalance α on the achieved SNR. The equations describing the operation of mixer with phase and amplitude balance imperfections are [31]

$$A_I(t) = A_G(t) \cos(\omega_{\text{LO}} t), \qquad \text{and} \qquad A_Q(t) = \alpha A_G(t) \sin(\omega_{\text{LO}} t + \varphi), \tag{2.44}$$

or in complex form

$$A_{\text{dc}}(t) = A_I(t) + i A_Q(t) = A_G(t) \left(1 - \frac{1 - \alpha e^{i\varphi}}{2} \right) e^{i\omega_{\text{LO}} t} + A_G(t) \frac{1 - \alpha e^{-i\varphi}}{2} e^{-i\omega_{\text{LO}} t}. \tag{2.45}$$

For conciseness we define the complex parameter $\varepsilon \equiv \frac{1-\alpha e^{i\varphi}}{2}$ that describes both the amplitude and phase imbalance. For an ideal mixer $\varepsilon = 0$.

In frequency domain the downconverted signal after filtering out frequency components with $|\omega| > \omega_{\mathrm{IF,max}}$ is

$$\begin{aligned} A_{\mathrm{dc}}(\omega) &= \frac{1}{\sqrt{2\pi}} \int_{-\infty}^{\infty} A_{\mathrm{dc}}(t) e^{i\omega t} \mathrm{d}t = (1-\varepsilon) A_G(\omega + \omega_{\mathrm{LO}}) + \varepsilon^* A_G(\omega - \omega_{\mathrm{LO}}) \\ &= (1-\varepsilon) V_0(\omega_{\mathrm{LO}} + \omega) a_G(\omega_{\mathrm{LO}} + \omega) + \varepsilon^* V_0(\omega_{\mathrm{LO}} - \omega) a_G^*(\omega_{\mathrm{LO}} - \omega) \end{aligned} \tag{2.46}$$

The effect of these mixer imperfections is the appearance of a second side-band at the frequency $\omega'_{\mathrm{IF}} = \omega_{\mathrm{LO}} - \omega_{\mathrm{RO}} = -\omega_{\mathrm{IF}}$.

If the parameter ε is known and we can discard the added noise during and after the down-conversion, this imperfection can be corrected for. In terms of the corrected signal $A'_{\mathrm{dc}}(\omega) = V_0(\omega_{\mathrm{LO}} + \omega) a_G(\omega_{\mathrm{LO}} + \omega)$, Eq. (2.46) is given as

$$A_{\mathrm{dc}}(\omega) = (1-\varepsilon) A'_{\mathrm{dc}}(\omega) + \varepsilon^* A'^*_{\mathrm{dc}}(-\omega). \tag{2.47}$$

This equation can be inverted to calculate the corrected signal in frequency and time domain

$$A'_{\mathrm{dc}}(\omega) = \frac{(1-\varepsilon^*) A_{\mathrm{dc}}(\omega) - \varepsilon^* A^*_{\mathrm{dc}}(-\omega)}{|1-\varepsilon|^2 - |\varepsilon|^2}, \tag{2.48a}$$

$$A'_{\mathrm{dc}}(t) = \frac{(1-\varepsilon^*) A_{\mathrm{dc}}(t) - \varepsilon^* A^*_{\mathrm{dc}}(t)}{|1-\varepsilon|^2 - |\varepsilon|^2}. \tag{2.48b}$$

In practice this inversion could be programmed into the integration weights. To take into account the mixer imperfection, we want to calculate the integrated signal with the mode-matched integration weights as

$$\mathcal{S} = \mathrm{Re}\left\{ \int_{-\pi\nu_{\mathrm{S}}}^{\pi\nu_{\mathrm{S}}} D'(\omega) \Delta D'^*(\omega) \mathrm{d}\omega \right\}, \tag{2.49}$$

where $D'(\omega) = \sqrt{\nu_{\mathrm{S}}} A'_{\mathrm{dc}}(\omega)$ is the Fourier transform of the digitized signal that has been corrected for the mixer imperfection (same as Eq. (2.25)) and $\Delta D'(\omega)$ is the average difference between the corrected signals for the qubit in the ground- and excited states. In terms of the uncorrected signals this equation is

$$\begin{aligned} \mathcal{S} &= \mathrm{Re}\left\{ \int_{-\pi\nu_{\mathrm{S}}}^{\pi\nu_{\mathrm{S}}} \frac{((1-\varepsilon^*) D(\omega) - \varepsilon^* D^*(-\omega))((1-\varepsilon)\Delta D^*(\omega) - \varepsilon \Delta D(-\omega))}{\left(|1-\varepsilon|^2 - |\varepsilon|^2\right)^2} \mathrm{d}\omega \right\} = \\ &= \mathrm{Re}\left\{ \int_{-\pi\nu_{\mathrm{S}}}^{\pi\nu_{\mathrm{S}}} D(\omega) \frac{(|1-\varepsilon|^2 + |\varepsilon|^2)\Delta D^*(\omega) - 2\varepsilon(1-\varepsilon^*)\Delta D(-\omega)}{\left(|1-\varepsilon|^2 - |\varepsilon|^2\right)^2} \mathrm{d}\omega \right\}. \end{aligned} \tag{2.50}$$

We see that the optimal weight function is

$$w(\omega) = \frac{(|1-\varepsilon|^2 + |\varepsilon|^2)\Delta D^*(-\omega) - 2\varepsilon(1-\varepsilon^*)\Delta D(\omega)}{\left(|1-\varepsilon|^2 - |\varepsilon|^2\right)^2} \tag{2.51a}$$

$$w[k] = \frac{(|1-\varepsilon|^2 + |\varepsilon|^2)\Delta D^*[k] - 2\varepsilon(1-\varepsilon^*)\Delta D[k]}{\left(|1-\varepsilon|^2 - |\varepsilon|^2\right)^2}. \tag{2.51b}$$

The time-domain Eq. (2.51b) assumes that the mixer imperfection is independent of frequency. In practice it might not be the case, in which case Eq. (2.51a) would have to be converted to time-domain with the general formula for the inverse Fourier transform.

Next we will calculate the loss of SNR if we do not correct for the mixer imperfection and use just the complex conjugate of the difference of digitized signal for the two qubit states as the weights $w(\omega) = \Delta D^*(-\omega)$. In this case the integrated signal and its variation are

$$\langle \mathcal{S}^e \rangle - \langle \mathcal{S}^g \rangle = \int_{-\pi\nu_\mathrm{S}}^{\pi\nu_\mathrm{S}} |\Delta D(\omega)|^2 \mathrm{d}\omega \tag{2.52a}$$

$$\left\langle \delta\mathcal{S}^2 \right\rangle = \int_{-\pi\nu_\mathrm{S}}^{\pi\nu_\mathrm{S}} \int_{-\pi\nu_\mathrm{S}}^{\pi\nu_\mathrm{S}} \langle \mathrm{Re}\{\delta D(\omega)\Delta D^*(\omega)\}\, \mathrm{Re}\{\delta D(\omega')\Delta D^*(\omega')\}\rangle \mathrm{d}\omega \mathrm{d}\omega'. \tag{2.52b}$$

To expand the real parts as a sum of the argument and its complex conjugate in Eq. (2.52b), we find the correlation terms

$$\langle \delta D(\omega)\delta D(\omega')\rangle = \nu_\mathrm{S}(1-\varepsilon)\varepsilon^* \Big(V_0^2 N\big|_{\omega_\mathrm{LO}+\omega} + V_0^2 N\big|_{\omega_\mathrm{LO}-\omega} \Big) \delta(\omega+\omega'), \tag{2.53a}$$

$$\langle \delta D(\omega)\delta D^*(\omega')\rangle = \nu_\mathrm{S} \Big(|1-\varepsilon|^2 V_0^2 N\big|_{\omega_\mathrm{LO}+\omega} + |\varepsilon|^2 V_0^2 N\big|_{\omega_\mathrm{LO}-\omega} \Big) \delta(\omega-\omega'). \tag{2.53b}$$

For clarity I will drop the dependence of V_0 and N on frequency, assuming that the IF is small compared to the LO frequency and that the noise has an uniform spectrum. Next to find the effect of mixer imperfections on the SNR, we want to express the signal and noise of the downconverted signal in terms of the signal $\Delta A_G(\omega)$ and noise $V_0^2 N$ of the amplified signal at the input of the mixer. For this I will assume that there is no overlap between the two side-bands in the input signal $|\Delta A_G(\omega_\mathrm{LO}+\omega)||\Delta A_G(\omega_\mathrm{LO}-\omega)| = 0$. This is true as long as the pulse spectrum is narrower than the intermediate frequency ω_IF used. In the case that there is overlap between the pulses, similar calculations can be done, but the result will be more complicated as it will depend on the amount of overlap. To find the expressions for signal and noise, we have to

evaluate the following integrals

$$\int_{-\pi\nu_\mathrm{S}}^{\pi\nu_\mathrm{S}} |\Delta D(\omega)|^2 \mathrm{d}\omega = \nu_\mathrm{S} \int_{-\pi\nu_\mathrm{S}}^{\pi\nu_\mathrm{S}} |(1-\varepsilon)\Delta A_G(\omega_\mathrm{LO}+\omega) + \varepsilon^* \Delta A_G(\omega_\mathrm{LO}-\omega)|^2 \mathrm{d}\omega =$$

$$= \nu_\mathrm{S}\big(|1-\varepsilon|^2 + |\varepsilon|^2\big) \int_{\omega_\mathrm{LO}-\pi\nu_\mathrm{S}}^{\omega_\mathrm{LO}+\pi\nu_\mathrm{S}} |\Delta A_G(\omega)|^2 \mathrm{d}\omega, \tag{2.54a}$$

$$\int_{-\pi\nu_\mathrm{S}}^{\pi\nu_\mathrm{S}} \Delta D(\omega)\Delta D(-\omega)\mathrm{d}\omega = 2\nu_\mathrm{S}(1-\varepsilon)\varepsilon^* \int_{\omega_\mathrm{LO}-\pi\nu_\mathrm{S}}^{\omega_\mathrm{LO}+\pi\nu_\mathrm{S}} |\Delta A_G(\omega)|^2 \mathrm{d}\omega. \tag{2.54b}$$

Combining the results from Eqs. (2.53a) to (2.54b), we find the signal and noise to be

$$\langle \mathcal{S}^e \rangle - \langle \mathcal{S}^g \rangle = \nu_\mathrm{S}\big(|1-\varepsilon|^2 + |\varepsilon|^2\big) \int_{\omega_\mathrm{LO}-\pi\nu_\mathrm{S}}^{\omega_\mathrm{LO}+\pi\nu_\mathrm{S}} |\Delta A_G(\omega)|^2 \mathrm{d}\omega, \tag{2.55a}$$

$$\big\langle \delta\mathcal{S}^2 \big\rangle = \frac{\nu_\mathrm{S}^2 V_0^2 N}{2}\Big(\big(|1-\varepsilon|^2 + |\varepsilon|^2\big)^2 + 4|1-\varepsilon|^2|\varepsilon|^2\Big) \int_{\omega_\mathrm{LO}-\pi\nu_\mathrm{S}}^{\omega_\mathrm{LO}+\pi\nu_\mathrm{S}} |\Delta A_G(\omega)|^2 \mathrm{d}\omega. \tag{2.55b}$$

The SNR is therefore

$$\mathrm{SNR}^2 = \frac{(\langle \mathcal{S}^e \rangle - \langle \mathcal{S}^g \rangle)^2}{\langle \delta\mathcal{S}^2 \rangle} = \frac{\big(|1-\varepsilon|^2 + |\varepsilon|^2\big)^2}{\big(|1-\varepsilon|^2 + |\varepsilon|^2\big)^2 + 4|1-\varepsilon|^2|\varepsilon|^2} \frac{2\int_{\omega_\mathrm{LO}-\pi\nu_\mathrm{S}}^{\omega_\mathrm{LO}+\pi\nu_\mathrm{S}} |\Delta A_G(\omega)|^2 \mathrm{d}\omega}{V_0^2 N}. \tag{2.56}$$

The first factor on the right hand side of Eq. (2.56) gives the reduction of the SNR due to the imperfection while the second factor is the available SNR in the signal before downconversion. We define the mixer efficiency $\eta_\mathrm{mix.}$ as the ratio of signal to noise ratios

$$\eta_\mathrm{mix.} = \frac{\mathrm{SNR}^2}{\mathrm{SNR}^2_{\varepsilon=0}} = \left(1 + 4\frac{|1-\varepsilon|^2|\varepsilon|^2}{\big(|1-\varepsilon|^2 + |\varepsilon|^2\big)^2}\right)^{-1} = \frac{(1+\alpha^2)^2}{2\big(1 + 2\alpha^2\sin^2(\varphi) + \alpha^4\big)} \tag{2.57}$$

For example with amplitude imbalance $\alpha = 1\,\mathrm{dB}$ and phase imbalance $\varphi = 5°$, the efficiency would be $\eta_\mathrm{mix.} = 94\,\%$. When only a single ADC channel is available, a mixer with only one output is sometimes used. This corresponds to the case $\alpha = 0$ where mixer efficiency is $\eta_\mathrm{mix.} = 1/2$ and half the signal is lost.

2.4 Multiplexed readout

Reading out several qubits at the same time using frequency-multiplexing is in many ways similar to reading out a single qubit. The basic principle is sketched in Fig. 3. Instead of applying a square pulse modulated at some carrier frequency ω_RO to the input of the device, we apply a sum

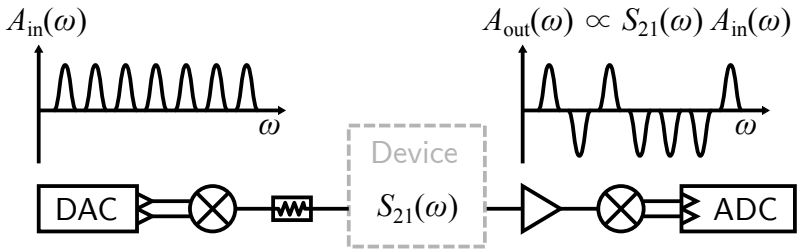

Figure 3: A circuit diagram depicting the architecture we use for multiplexed readout. The spectra of the readout pulse at the input and output of the device are depicted in the top left and right corners.

of pulses with different modulation frequencies $\omega_{\text{RO},j}$ and possibly different amplitudes A_j. The multi-tone readout signal can be generated by upconverting two baseband signals, representing the real and imaginary part of a complex signal, using an IQ-mixer. Given the inputs $A_I(t)$ and $A_Q(t)$ of the mixer, the output of the mixer, which is the input to the cryostat, is

$$A_{\text{in}}(t) = A_I(t)\cos(\omega_{\text{LO}}t) - A_Q(t)\sin(\omega_{\text{LO}}t) = \text{Re}\big\{(A_I(t) + iA_Q(t))e^{i\omega_{\text{LO}}t}\big\}, \tag{2.58}$$

where ω_{LO} is the local oscillator frequency. By choosing the intermediate frequencies of the different tones $\omega_{\text{IF},j} = \omega_{\text{RO},j} - \omega_{\text{LO}}$, we find the readout signal as the sum over the readout tones

$$A_{\text{in}}(t) = \sum_j \text{Re}\big\{(A_j\cos(\omega_{\text{IF},j}t) + iA_j\sin(\omega_{\text{IF},j}t))e^{i\omega_{\text{LO}}t}\big\} = \sum_j \text{Re}\big\{A_j e^{i\omega_{\text{RO},j}t}\big\}. \tag{2.59}$$

The multi-tone signal enables us to probe the transmission spectrum $S_{21}(\omega)$ at several different frequencies at the same time. By choosing the readout resonators of the different qubits $\mathsf{Q}j$ to have unique frequencies $\omega_{\text{R},j}$, we encode the information about the state of the different qubits in different frequency ranges of $S_{21}(\omega)$. Finally, to discriminate between all the qubit states, we need to have different integration weights $w_j[k]$ for each qubit resulting in the integration results $\mathcal{S}_j$. From Eq. (2.28a) we see that the integration weights $w_j(-\omega)$ of qubit $\mathsf{Q}j$ need to have spectral overlap with the difference of the transmission spectra for $\mathsf{Q}j$ in the ground and excited state $\Delta_j S_{21}(\omega_{\text{LO}} + \omega)$. Here and in the following Δ_j represents the average difference between the signals for qubit $\mathsf{Q}j$ in the excited and in the ground state.

The amount of qubits that can be read out using frequency multiplexing is limited by the available bandwidth of the different parts of the readout chain, the bandwidth of a single qubit's readout resonator and the dynamic range of the amplification chain. In our setup the bandwidth of the measurement chain is limited by the digital-analog converter (DAC) and ADC instrument

at $2 \times 600\,\mathrm{MHz}$. Another critical part of the measurement chain that might limit the available bandwidth is the first amplifier. The widely used Josephson parametric dimer amplifiers, for example, have bandwidth in the order of 30 MHz [32]. We use a travelling wave parametric amplifier (TWPA) [33], which has high gain $G > 20\,\mathrm{dB}$ over a 3 GHz bandwidth. Because high-bandwidth IQ-mixers and secondary amplifiers are commercially available, they should not be limiting the bandwidth of the measurement chain. The dynamic range of an amplifier can become the limiting factor for increasing the number of qubits when the total power of the different readout tones approaches the 1 dB compression point of one of the amplifiers or mixers.

2.4.1 Characterizing crosstalk

In this subsection we discuss different methods to characterize the crosstalk in multiplexed readout. For the corresponding experimental results, see also Section 4.2.

The goodness of single qubit readout is characterized by its *fidelity*

$$F \equiv 1 - P(e \mid 0) - P(g \mid \pi), \tag{2.60}$$

where e and g denote the measurement result and 0 and π denote the preparation, g and 0 corresponding to the ground state and e and π to the excited state. To experimentally measure the fidelity, the qubit is repeatedly prepared in one of the states and then measured, recording the histograms of the integration results for both preparations. By normalizing the histograms to unit area we find the probability densities of the results $p(\mathcal{S}) = \left.\frac{\mathrm{d}P(\mathcal{S}<\mathcal{S}_0)}{\mathrm{d}\mathcal{S}_0}\right|_{\mathcal{S}_0=\mathcal{S}}$, where we have denoted the probability that the integrated result is less than some value $\mathcal{S}_0$ as $P(\mathcal{S} < \mathcal{S}_0)$. The threshold value $\mathcal{S}_{\mathrm{th.}}$ is then chosen as the solution of $p(\mathcal{S} \mid 0) = p(\mathcal{S} \mid \pi)$ to maximize the fidelity. The main contributors to the infidelity terms $P(e \mid 0)$ and $P(g \mid \pi)$ are noise in the integrated signal, making the distributions $p(\mathcal{S} \mid 0)$ and $p(\mathcal{S} \mid \pi)$ overlap; qubit decay during the measurement; and qubit state mixing during measurement, causing both qubit excitation and decay. [34]

To characterize multiplexed readout of n qubits, one can also measure the probability densities of the integration results for the different preparations $(\zeta_1 ... \zeta_n) \in \{0, \pi\}^n$. By classifying the integration results based on the threshold values $\mathcal{S}_{\mathrm{th.},j}$, we get a $2^n \times 2^n$ *assignment probability matrix* $P(s_1 ... s_n \mid \zeta_1 ... \zeta_n)$, where $(s_1 ... s_n) \in \{g, e\}^n$ are the classification results. The assignment probability matrix will deviate from the ideal diagonal matrix already because of the single qubit

errors mentioned in the previous paragraph. In addition to the single qubit errors, there might be correlations between the measurement results of different qubits. In the ideal case with no crosstalk, the joint probability distribution would be the product of the marginal distributions

$$P(s_1...s_n \mid \zeta_1...\zeta_n) = P(s_1 \mid \zeta_1)...P(s_n \mid \zeta_n). \tag{2.61}$$

Qualitatively, readout crosstalk is the deviation of the assignment probability matrix from the separable form (2.61).

There are several options to quantify the amount of correlation between different qubits. Looking at the difference between the measured assignment probability matrix and the uncorrelated one that is the product of the marginal distributions, one can see all orders of correlation. For example correlations in the decay of different qubits can be detected. Another metric to look at is the correlation between the preparation and measurement results of different qubits. We define the cross-fidelity F_{ij} between qubits $\mathsf{Q}i$ and $\mathsf{Q}j$ as

$$F_{ij} \equiv \langle \zeta_i s_j \rangle = 1 - P(e_j \mid 0_i) - P(g_j \mid \pi_i). \tag{2.62}$$

The diagonal elements $i = j$ give the standard definition of the single qubit readout fidelity [34]. The advantage of looking at the average correlations is that the full table has only n^2 unique elements – one for each ordered qubit pair, compared to the 4^n elements of the full assignment probability matrix. However information about some types of correlations, for example correlated bit-flip errors, are lost in the process of averaging over the preparation states.

So far we have looked at the crosstalk between different qubits that we are measuring. In some applications we only want to measure a subset of the qubits that are connected to the same input and output port of the device, and not affect the quantum state of the other qubits. One way to characterize this type of crosstalk would be to use process tomography [35] or gate-set tomography [36] to find the corresponding process matrix on the unmeasured qubit. A simpler way to characterize this effect is to measure only the dephasing of the unmeasured qubit, which is expected to be the dominant effect. This is done in the *cross-Ramsey dephasing* experiment [37], where the measurement pulse is sandwiched between two $\pi/2$ pulses on the unmeasured qubit. While varying the phase of the second $\pi/2$ pulse, we record the contrast of the oscillating integrated signal $\mathcal{S}$. The loss in contrast is proportional to the exponent of the total dephasing of the qubit Γ. To show this we look at the evolution of the state of the

unmeasured qubit in the density matrix formalism:

$$\hat{\rho}_{\mathrm{i}} = |g\rangle\langle g| = \begin{pmatrix} 1 & 0 \\ 0 & 0 \end{pmatrix} \xrightarrow{\text{first } \pi/2 \text{ pulse}} \frac{1}{2}\begin{pmatrix} 1 & -i \\ i & 1 \end{pmatrix} \xrightarrow{\text{dephasing}} \frac{1}{2}\begin{pmatrix} 1 & -ie^{-\Gamma} \\ ie^{-\Gamma} & 1 \end{pmatrix}$$
$$\xrightarrow[\text{around angle } \phi]{\text{second } \pi/2 \text{ pulse}} \frac{1}{2}\begin{pmatrix} 1 - e^{-\Gamma}\cos(\phi) & e^{-\Gamma - i\phi}\sin(\phi) \\ e^{-\Gamma + i\phi}\sin(\phi) & 1 + e^{-\Gamma}\cos(\phi) \end{pmatrix} = \hat{\rho}_{\mathrm{f}}. \tag{2.63}$$

The averaged integrated measurement result, normalized such that $\mathcal{S} = 1$ for qubit in the ground state and $\mathcal{S} = -1$ for the qubit in the excited state, is then $\mathrm{tr}(\hat{\sigma}_z \rho_{\mathrm{f}}) = -e^{-\Gamma}\cos(\phi)$. We extract the dephasing Γ from the amplitude $e^{-\Gamma}$ of the oscillations as a function of ϕ.

2.4.2 Causes of crosstalk

In the previous subsection we discussed the different ways to recognize and quantify the crosstalk in multiplexed readout, but said nothing about the physical origins leading to the crosstalk. The mechanisms can be roughly divided into 5 categories, that we will present in this subsection.

Preparation crosstalk Typically state preparation and measurement errors are hard to distinguish, since bit-flip errors during them look identical in the measurement results. This notion also carries on to correlations between state preparation and measurement errors. We call the correlations in measurement results that arises due to crosstalk in the state preparation *preparation crosstalk*. If the preparation pulse of qubit $\mathsf{Q}i$ also couples to qubit $\mathsf{Q}j$, we would see an increased number of bit-flips on $\mathsf{Q}j$ if $\mathsf{Q}i$ was prepared in the excited state. This effect would however not be visible in cross-fidelity F_{ij}, as the effects of putting $\mathsf{Q}j$ in the excited state and putting it in the ground state cancel out. To determine the magnitude of the expected preparation crosstalk, Rabi oscillation can be driven using another qubit's drive line. The ratio of pulse amplitudes needed to do a π-pulse gives the ratio of the coupling rates to the two ports. The effect of the preparation pulse on the other qubit can be estimated from the preparation pulse parameters and the cross-coupling. Another example of a cause for state preparation crosstalk would be a $\hat{\sigma}_z^i \hat{\sigma}_z^j$ interaction between the two qubits.

Direct cross-coupling In the Jaynes-Cummings Hamiltonian (2.1) we have the coupling strength g between the qubit and the readout resonator. If a qubit $\mathsf{Q}i$ and the resonator $\mathsf{R}j$ of

an other qubit $\mathsf{Q}j$ are physically situated close to each other, or if they both couple to a spurious mode on the device, a *direct cross-coupling* term might appear in the Hamiltonian:

$$\hat{H}_{\mathrm{xc}} = \hbar g_{ij}(\hat{a}^{\dagger}_{\mathrm{R}j}\hat{\sigma}_{\mathrm{Q}i} + \hat{a}_{\mathrm{R}j}\hat{\sigma}^{\dagger}_{\mathrm{Q}i}). \tag{2.64}$$

In the dispersive regime, this gives rise to cross-dispersive shift χ_{ij} that changes the resonator $\mathsf{R}j$ frequency depending on the state of $\mathsf{Q}i$. This type of crosstalk would be apparent in the cross-Ramsey dephasing measurement as populating $\mathsf{R}j$ can be seen as a weak measurement of $\mathsf{Q}i$. To do a more direct measurement of the direct cross-coupling and the cross-dispersive shift, one can measure the transmission spectrum of $\mathsf{R}j$ and check if the resonance is shifted between the two states of $\mathsf{Q}i$. In practical realizations we don't expect the direct cross-coupling to be significant as the qubits are physically located relatively far from other readout resonators.

Spectral overlap Another possible mechanism causing dephasing visible in the cross-Ramsey measurement is a *spectral overlap* between the readout pulse of qubit $\mathsf{Q}i$ and the readout resonator $\mathsf{R}j$ of another qubit. In this case the readout pulse populates the resonator $\mathsf{R}j$ with photons which in turn leads to dephasing of $\mathsf{Q}j$. To avoid the spectral overlap, the sum of the spectral width of the pulse, characterized by the inverse pulse-length $1/\tau_i$, and the width of the resonator spectrum, characterized by the decay rate $\kappa_{\mathrm{R},j}$, should be much greater than the frequency spacing between the readout resonators $1/\tau_i + \kappa_{\mathrm{R},j} \gg |\omega_{\mathrm{R},i} - \omega_{\mathrm{R},j}|$.

Signal crosstalk In the general case we could have 2^n different transmission spectra $S^s_{21}(\omega)$, depending on the state s of the n-qubit system. The state-dependent transmission can be written as a function of the $\hat{\sigma}_z$ operators:

$$S_{21}(\omega) = \left\langle S^s_{21}(\omega)\prod_{i=1}^{n}(1 + s_i\hat{\sigma}^i_z)\right\rangle_s = \langle S^s_{21}(\omega)\rangle_s + \sum_{i=1}^{n}\sigma^i_z\langle s_i S^s_{21}(\omega)\rangle_s + \\ + \frac{1}{2}\sum_{\substack{i,j=1\\ i\neq j}}^{n}\sigma^i_z\sigma^j_z\langle s_i s_j S^s_{21}(\omega)\rangle_s + \ldots \tag{2.65}$$

The averages are taken over all the possible computational basis states s of the n-qubit system. The variables $s_i = 1$ for the qubit $\mathsf{Q}i$ in the ground state and $s_i = -1$ for the qubit in the excited

state. By truncating the series at the second term, we come to the expression

$$S_{21}(\omega) \approx \bar{S}_{12}(\omega) - \frac{1}{2}\sum_{j=1}^{n} \sigma_z^j \Delta_j S_{21}(\omega), \tag{2.66}$$

where we have introduced the average transmission amplitude $\bar{S}_{12}(\omega) \equiv \langle S_{21}^s(\omega)\rangle_s$ and the average difference in the transmission amplitude for qubit $\mathsf{Q}j$ in the excited and ground state $\Delta_j S_{21}(\omega)$. This truncation is exact if the resonances in the transmission spectrum don't overlap, but is a good approximation even with some overlap present. The integrated results are then

$$\mathcal{S}_i = \bar{\mathcal{S}}_i + \sum_{j=1}^{n} \mathcal{M}_{ij}\sigma_z^j, \tag{2.67}$$

where we use Eq. (2.28a) to find the matrix elements to be

$$\bar{\mathcal{S}}_i = \sqrt{AG\nu_\mathrm{S}} \int_{\omega_\mathrm{LO}-\pi\nu_\mathrm{s}}^{\omega_\mathrm{LO}+\pi\nu_\mathrm{s}} V_0(\omega)\,\mathrm{Re}\Big\{\bar{S}_{21}(\omega)\Big\langle \hat{b}_\mathrm{in}(\omega)\Big\rangle w_i(\omega_\mathrm{LO}-\omega)\Big\}\mathrm{d}\omega, \tag{2.68a}$$

$$\mathcal{M}_{ij} = -\frac{\sqrt{AG\nu_\mathrm{S}}}{2} \int_{\omega_\mathrm{LO}-\pi\nu_\mathrm{s}}^{\omega_\mathrm{LO}+\pi\nu_\mathrm{s}} V_0(\omega)\,\mathrm{Re}\Big\{\Delta S_{21}^j(\omega)\Big\langle \hat{b}_\mathrm{in}(\omega)\Big\rangle w_i(\omega_\mathrm{LO}-\omega)\Big\}\mathrm{d}\omega. \tag{2.68b}$$

We see that spectral overlap between the change in transmission $\Delta_j S_{21}(\omega)$ due to the state of $\mathsf{Q}j$ and the integration weights $w_i(\omega_\mathrm{LO}-\omega)$ of $\mathsf{Q}i$ results in non-diagonal elements $\mathcal{M}_{ij}$ and *signal crosstalk*. By inverting the matrix $\mathcal{M}$, we can transform the integration results $\mathcal{S}_i$ to a set $\mathcal{S}_i'$ dependant on the state of a single qubit only

$$\mathcal{S}_i' = \sum_{j=1}^{n} \big(\mathcal{M}^{-1}\big)_{ij}\mathcal{S}_j = \sum_{j=1}^{n} \big(\mathcal{M}^{-1}\big)_{ij}\bar{\mathcal{S}}_j + \sigma_z^i. \tag{2.69}$$

This means that we can always get rid of signal crosstalk up to the accuracy of the truncation in Eq. (2.66).

Environment-induced crosstalk There can also be a deviation from the separable form of the assignment probability matrix Eq. (2.61) even if there are no cross-couplings of the elements on the device and if the readout itself is perfectly crosstalk free. To illustrate this, let's look at an exaggerated example of two qubit multiplexed readout. Let us, for the first half of the measurement, have perfect measurement with a diagonal probability assignment matrix P_1, but

for second half of the measurement, due to an external noise, all the qubits are in the mixed state, resulting in a uniform matrix P_2:

$$P_1 = \begin{array}{c} \\ 00 \\ 0\pi \\ \pi 0 \\ \pi\pi \end{array} \begin{array}{c} \begin{array}{cccc} gg & ge & eg & ee \end{array} \\ \begin{pmatrix} 1 & 0 & 0 & 0 \\ 0 & 1 & 0 & 0 \\ 0 & 0 & 1 & 0 \\ 0 & 0 & 0 & 1 \end{pmatrix} \end{array}, \qquad P_2 = \frac{1}{4} \begin{array}{c} \\ 00 \\ 0\pi \\ \pi 0 \\ \pi\pi \end{array} \begin{array}{c} \begin{array}{cccc} gg & ge & eg & ee \end{array} \\ \begin{pmatrix} 1 & 1 & 1 & 1 \\ 1 & 1 & 1 & 1 \\ 1 & 1 & 1 & 1 \\ 1 & 1 & 1 & 1 \end{pmatrix} \end{array} \tag{2.70}$$

The average probability assignment matrix for this measurement is then

$$P_3 = \frac{P_1 + P_2}{2} = \frac{1}{8} \begin{array}{c} \\ 00 \\ 0\pi \\ \pi 0 \\ \pi\pi \end{array} \begin{array}{c} \begin{array}{cccc} gg & ge & eg & ee \end{array} \\ \begin{pmatrix} 5 & 1 & 1 & 1 \\ 1 & 5 & 1 & 1 \\ 1 & 1 & 5 & 1 \\ 1 & 1 & 1 & 5 \end{pmatrix} \end{array}, \tag{2.71}$$

which is not separable to two individual probability matrices. If the two qubit assignment probability matrices were independent with the same marginal distributions, we would have the probability matrix

$$P_4 = \frac{1}{16} \begin{array}{c} \\ 00 \\ 0\pi \\ \pi 0 \\ \pi\pi \end{array} \begin{array}{c} \begin{array}{cccc} gg & ge & eg & ee \end{array} \\ \begin{pmatrix} 9 & 3 & 3 & 1 \\ 3 & 9 & 1 & 3 \\ 3 & 1 & 9 & 3 \\ 1 & 3 & 3 & 9 \end{pmatrix} \end{array} = P_3 - \frac{1}{16} \begin{array}{c} \\ 00 \\ 0\pi \\ \pi 0 \\ \pi\pi \end{array} \begin{array}{c} \begin{array}{cccc} gg & ge & eg & ee \end{array} \\ \begin{pmatrix} -1 & 1 & 1 & -1 \\ 1 & -1 & -1 & 1 \\ 1 & -1 & -1 & 1 \\ -1 & 1 & 1 & -1 \end{pmatrix} \end{array}. \tag{2.72}$$

The environment crosstalk manifests itself as anti-correlation between bit-flip errors in this case.

2.4.3 Low-crosstalk device design

A crucial part of designing a device for multiplexed readout is developing accurate model for the transmission amplitude $S_{21}(\omega)$ as a function of the device parameters. In this subsection I summarise the results on the input-output relations of the device developed for fast low crosstalk multiplexed readout, investigated by J. Heinsoo [38].

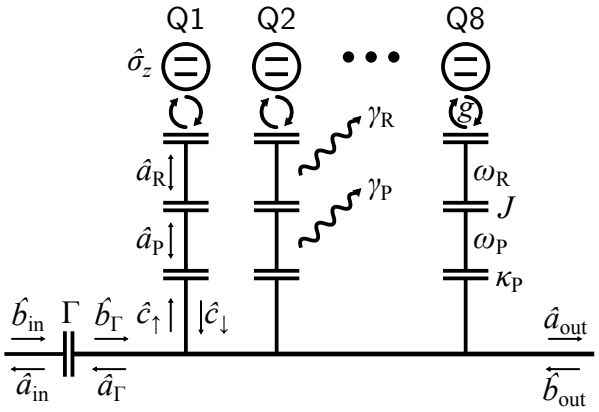

Figure 4: A schematic of the model used for calculating the input-output relations of the device designed for multiplexed readout.

As seen in Fig. 4, each of the qubits $\mathsf{Q}i$ has a readout resonator with a frequency $\omega_{\mathrm{R},i}$ coupled to it with rate g_i. The readout resonator is coupled to another resonator at frequency $\omega_{\mathrm{P},i}$, called *Purcell filter*, with coupling rate J_i that is in turn connected to a half-feedline with a rate $\kappa_{\mathrm{P},i}$. Adding the Purcell filter to the system changes the asymptotic behaviour of the transmission amplitude through the readout resonator at large detunings Δ from the resonator frequency from $1/\Delta$ to $1/\Delta^2$. This serves two purposes: First, it reduces the density of bosonic modes that the qubit sees from the continuum of the half-feedline, increasing the lifetime of the qubit. Second, it increases the suppression of the transmission amplitude difference $\Delta S_{21}(\omega)$ for the two qubit states at high detunings from the resonance. As we saw in Subsection 2.4.2, this is a requirement for low crosstalk readout. At the input side, the half-feedline is terminated by an capacitor, while at the output side it is galvanically coupled to direct the readout signal to the output port.

To find the transmission amplitude $S_{21}(\omega) = \hat{a}_{\mathrm{out}}(\omega)/\hat{b}_{\mathrm{in}}(\omega)$ for a single qubit connected to the half-feedline, we write down the input-output relations for the individual components on the device in frequency domain. We assume that the spectral width of the resonances is small enough that we can look at the resonators of a single qubit at a time.

The input capacitor with capacitance C_{in} has a reflection coefficient $\Gamma(\omega) = \frac{1}{1+2i\omega C_{\mathrm{in}} Z_0} = \frac{1-e^{i\alpha}}{2}$, where we have introduced an angle parameter $\cot\left(\frac{\alpha}{2}\right) = 2\omega C_{\mathrm{in}} Z_0$. The field $\hat{b}_\Gamma$ on the other side of the capacitor (see Fig. 4) is given by

$$\hat{b}_\Gamma(\omega) = (1 - \Gamma(\omega))\hat{b}_{\mathrm{in}}(\omega) + \Gamma \hat{a}_\Gamma(\omega). \tag{2.73}$$

The Purcell filter is connected to the half-feedline by a t-junction, giving the relations

$$\hat{c}_{\uparrow}(\omega) = -\frac{1}{3}\hat{c}_{\downarrow}(\omega) + \frac{2}{3}\hat{b}_{\Gamma}(\omega) + \frac{2}{3}\hat{b}_{\text{out}}(\omega), \tag{2.74a}$$

$$\hat{a}_{\Gamma}(\omega) = \frac{2}{3}\hat{c}_{\downarrow}(\omega) - \frac{1}{3}\hat{b}_{\Gamma}(\omega) + \frac{2}{3}\hat{b}_{\text{out}}(\omega), \tag{2.74b}$$

$$\hat{a}_{\text{out}}(\omega) = \frac{2}{3}\hat{c}_{\downarrow}(\omega) + \frac{2}{3}\hat{b}_{\Gamma}(\omega) - \frac{1}{3}\hat{b}_{\text{out}}(\omega). \tag{2.74c}$$

With the interaction Hamiltonian $\hat{H}_J = \hbar J(\hat{a}_{\text{R}}\hat{a}_{\text{P}}^{\dagger} + \hat{a}_{\text{R}}^{\dagger}\hat{a}_{\text{P}})$, and internal loss rates γ_{R} and γ_{P} the equations of motion for the two resonators are

$$0 = -i(\omega_{\text{R}} - \omega - \chi\sigma_z)\hat{a}_{\text{R}}(\omega) - iJ\hat{a}_{\text{P}}(\omega) - \frac{\gamma_{\text{R}}}{2}\hat{a}_{\text{R}}(\omega), \tag{2.75a}$$

$$0 = -i(\omega_{\text{P}} - \omega)\hat{a}_{\text{P}}(\omega) - iJ\hat{a}_{\text{R}}(\omega) - \frac{\gamma_{\text{P}} + \kappa_{\text{P}}}{2}\hat{a}_{\text{P}}(\omega) - \sqrt{\kappa_{\text{P}}}\hat{c}_{\uparrow}(\omega). \tag{2.75b}$$

The boundary condition, connecting the output field from the Purcell filter to the t-connector is

$$\hat{c}_{\downarrow}(\omega) = \hat{c}_{\uparrow}(\omega) + \sqrt{\kappa_{\text{P}}}\hat{a}_{\text{P}}(\omega). \tag{2.76}$$

The addition of the t-connector and the input capacitor to the system adds an additional port to the Purcell filter with which it interacts. This renormalizes the frequency and the linewidth of the filter to the values $\tilde{\kappa}_{\text{P}}$ and $\tilde{\omega}_{\text{P}}$:

$$\tilde{\kappa}_{\text{P}} = \kappa_{\text{P}}\frac{1 + \text{Re}\{\Gamma\}}{2} = \kappa_{\text{P}}\frac{3 - \cos(\alpha)}{4}, \tag{2.77a}$$

$$\tilde{\omega}_{\text{P}} = \omega_{\text{P}} + \kappa_{\text{P}}\frac{\text{Im}\{\Gamma\}}{4} = \omega_{\text{P}} - \kappa_{\text{P}}\frac{\sin(\alpha)}{8}. \tag{2.77b}$$

Solving the linear system of equations (2.73) to (2.76), we find the transmission amplitude to be

$$\frac{S_{21}(\omega)}{1-\Gamma} - 1 = -\left(\frac{1+\Gamma}{1+\text{Re}\{\Gamma\}}\right)\frac{\tilde{\kappa}_{\text{P}}(\gamma_{\text{R}} - 2i(\omega - \omega_{\text{R}} + \chi\sigma_z))}{4J^2 + (\gamma_{\text{P}} + \tilde{\kappa}_{\text{P}} - 2i(\omega - \tilde{\omega}_{\text{P}}))(\gamma_{\text{R}} - 2i(\omega - \omega_{\text{R}} + \chi\sigma_z))}. \tag{2.78}$$

We will later fit this form of the transmission amplitude to experimental data to find the system parameters ω_{R}, $\tilde{\omega}_{\text{P}}$, χ, and $\tilde{\kappa}_{\text{P}}$. For zero detuning between the two resonators $\Delta_{\text{RP}} = \omega_{\text{R}} - \tilde{\omega}_{\text{P}} = 0$ the spectrum consists a peak in the middle of a wider dip as seen in Fig. 5

For fast readout it is important to populate the readout resonator quickly. This speed is determined by the effective linewidth of the readout resonator κ_{R}. To find the effective linewidth

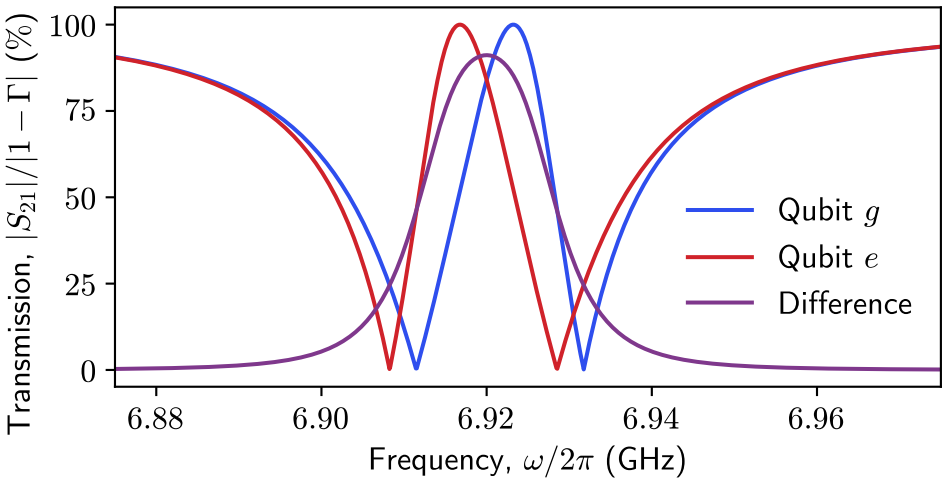

Figure 5: Transmission amplitude through the half-feedline for the qubit in the ground and excited state and the modulus of the difference of the two complex transmission amplitudes. Calculated according to the model (2.78) with the parameters $\Gamma = 1$, $\tilde{\omega}_\mathrm{P} = \omega_\mathrm{R} = 2\pi \times 6.92\,\mathrm{GHz}$, $\tilde{\kappa}_\mathrm{P} = 2\pi \times 40\,\mathrm{MHz}$, $\chi = -2\pi \times 3.23\,\mathrm{MHz}$, $J = 2\pi \times 10\,\mathrm{MHz}$, $\gamma_\mathrm{R} = \gamma_\mathrm{P} = 0$.

we write the equations of motion for the two resonator modes in time-domain and matrix form and set the inputs to zero $\hat{b}_\mathrm{in}(t) = \hat{b}_\mathrm{out}(t) = 0$:

$$\begin{pmatrix} \dot{\hat{a}}_\mathrm{R}(t) \\ \dot{\hat{a}}_\mathrm{P}(t) \end{pmatrix} = \begin{pmatrix} -\frac{\gamma_\mathrm{R}}{2} - i(\omega_\mathrm{R} - \sigma_z\chi) & -iJ \\ -iJ & -\frac{\gamma_\mathrm{P}+\tilde{\kappa}_\mathrm{P}}{2} - i\tilde{\omega}_\mathrm{P} \end{pmatrix} \begin{pmatrix} \hat{a}_\mathrm{R}(t) \\ \hat{a}_\mathrm{P}(t) \end{pmatrix}. \tag{2.79}$$

The decay rates κ of the eigenmodes of this coupled system are given by $\kappa = -2\,\mathrm{Re}\{\mathrm{E.V.}\}$, where E.V. is an eigenvalue of the square matrix in Eq. (2.79). For readout purposes we are interested in the effective linewidth κ_R of the mode that becomes the readout resonator mode in the $J \to 0$ limit. To keep the model simple, we look at the case of lossless resonators $\gamma_\mathrm{P} = \gamma_\mathrm{R} = 0$, to find the effective readout resonator linewidth

$$\kappa_\mathrm{R} = \frac{1}{2}\left(\tilde{\kappa}_\mathrm{P} - \mathrm{Re}\left\{\sqrt{(\tilde{\kappa}_\mathrm{P} + 2i(\tilde{\omega}_\mathrm{P} - \omega_\mathrm{R} + \chi\sigma_z))^2 - 16J^2}\right\}\right). \tag{2.80}$$

We see that to keep κ_R large, we need to keep the detuning between the readout resonator and the Purcell filter Δ_RP small.

In the following sections we will use the symbols κ_P and ω_P without the tilde to refer to the renormalized frequency and linewidth of the Purcell filter and also omit explicitly noting in the text that the renormalized values are meant.

3 Experimental setup

In this chapter I give a brief overview of the devices used in the course of this project and the experimental setup to operate these devices.

3.1 Devices used

Superconducting device fabrication and design were not in the scope of this project and were done by other members of the group. My contribution to the device development was the characterization of the test devices. Here I will give a brief overview of the different superconducting devices used over the course of my work.

All of the devices are fabricated on a sapphire substrate. A thin 150 nm film of niobium is sputtered on top of the substrate by a commercial supplier[1]. Next, the coplanar waveguide and coupling capacitor structure of the device and the qubit islands are etched out of the niobium using photolithography. Aluminum *airbridges* are fabricated over the coplanar waveguides to connect the different parts of the ground plane in two more steps of photolithography. For a more detailed description of the photolithography processes see the PhD thesis of L. Steffen [39]. The Josephson junctions necessary to create the qubits are fabricated using high precision electron beam lithography and shadow evaporation of aluminum. See the PhD thesis of J. Fink [40] for details.

It took several iterations of sample design to fabricate a device where we could implement multiplexed readout. In the first devices that implemented the readout geometry described in Subsection 2.4.3, we used a design where the qubits are formed from two superconducting islands connected by a SQUID loop. A false-colored micrograph of such an 8-qubit device is shown in Fig. 6a. One of the issues that stopped us from achieving fast high-fidelity single-shot readout on this device was the small effective linewidth κ_{R} of the readout resonators. There was a systematic detuning between the readout resonator and Purcell filter frequencies in the order of 15 MHz, which using Eq. (2.80) can be seen as one of the causes of the small effective linewidth. The challenge in fabricating resonators with accurate frequencies comes from the strong dependence of the resonance frequency on the different capacitances to the resonator. To

[1] STAR Cryoelectronics

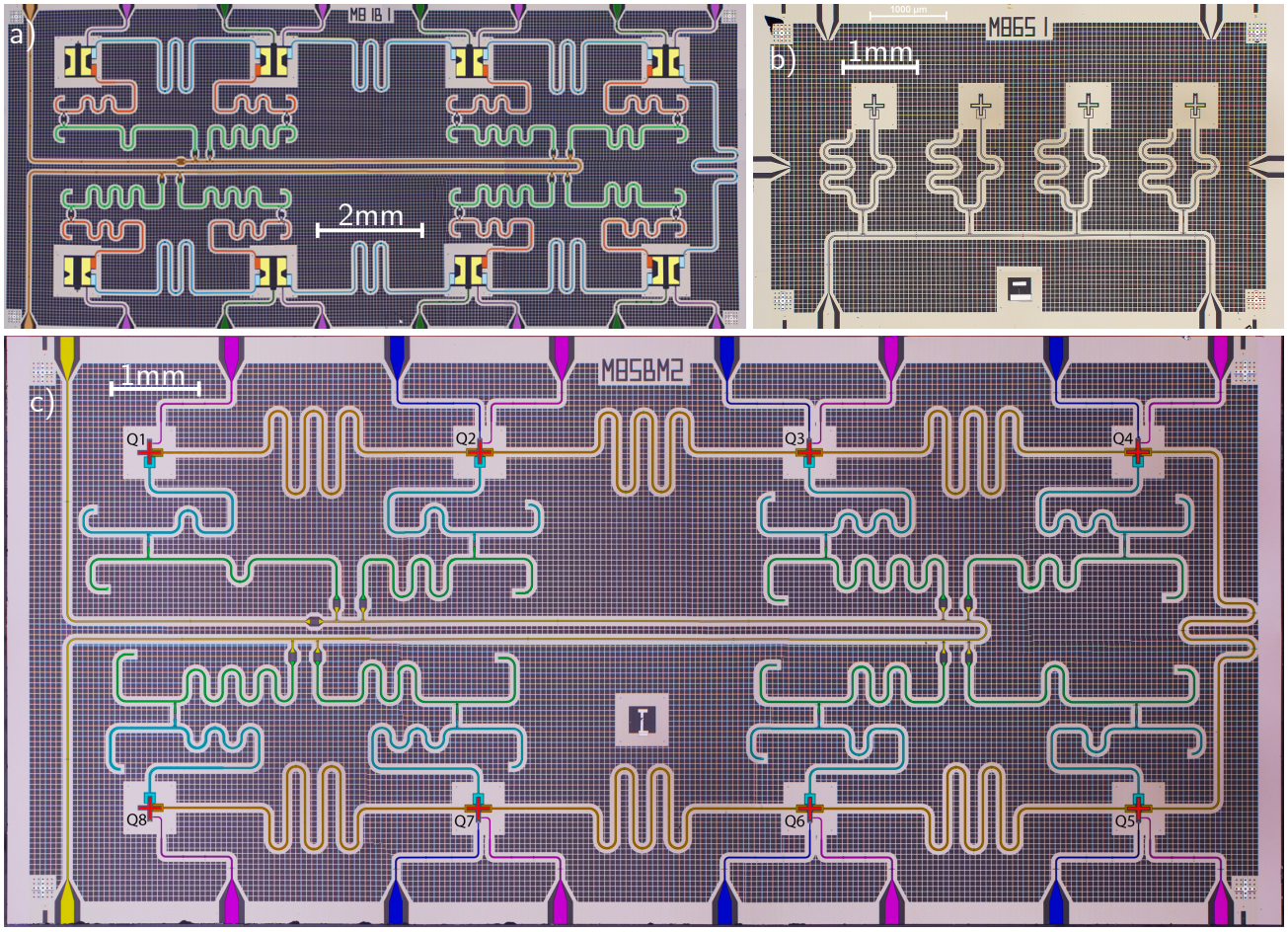

Figure 6: a), b) Micrographs of devices M81B1 and M86S1, used prior to the final device. c) A false color micrograph of the device M85BM2, used for multiplexed readout experiments. The color scheme is the same as in Fig. 1. In addition the Purcell filters are shown in green and the half-feedline is shown in yellow.

accurately predict the resonator frequency, the capacitances are modelled in an electrostatic finite element simulation using the ANSYS Maxwell software, and after that a capacitance network is solved to find the effective capacitance to the resonator.

To simplify the design of readout resonators and thereby improve the accuracy of their resonance frequencies, we moved to a new qubit design with a single island cross-shaped qubits [41]. One of the test samples can be seen in Fig. 6b. In addition to simplifying the capacitance network, the single-island qubit has the electric field more confined around the qubit compared to the two-island design. This could reduce the coupling to lossy elements in the sample-holder and the PCB, potentially increasing the qubit lifetime.

The main experiments of this thesis were done on the device M85BM2 shown in figure Fig. 6c. There are 8 single-island qubits, each with its individual readout resonator and Purcell filter. All of the Purcell filters are coupled to the half-feedline, which is galvanically coupled at the output port and capacitively coupled at the input port, implementing the readout structure from Subsection 2.4.3. All qubits, except for Q1 and Q8 have an individual flux bias line for tuning the qubit frequency with a dc current (see Eq. (2.3)) and for tuning transitions on different qubits into resonance with each other, implementing two-qubit gates [42]. The coupling between the qubits needed for implementing two-qubit gates is mediated by virtual photons in the coupling resonators between neighbouring qubits, forming a linear chain.

For multiplexed readout experiments we used only qubits Q2, Q3, Q5, Q6 and Q7, because the data acquisition device we used for multiplexed readout, the Zurich Instruments UHFLI, supported 5 weighted integration units. This choice of qubits was due to the fact that the qubits at the corners of the device, Q1, Q4, Q5 and Q8, had much higher maximum frequencies than designed. They would therefore have to be operated far from their *sweetspot* $\omega_{\mathrm{Q}} = \omega_{\mathrm{Q,max}}$, where the qubit's sensitivity to magnetic flux fluctuations through the SQUID loop $\frac{\partial \omega_{\mathrm{Q}}}{\partial \Phi}$ is large. The increased sensitivity increases the fluctuations of qubit frequency, causing dephasing of the qubit.

3.2 Cryogenics and wiring

To reduce noise in the environment and thereby increase the coherence of the qubits, the quantum device is cooled down to around 10 mK in a dilution refrigerator by BlueFors. We use the low temperature of the device also for state preparation as the thermal state of the qubit is close to

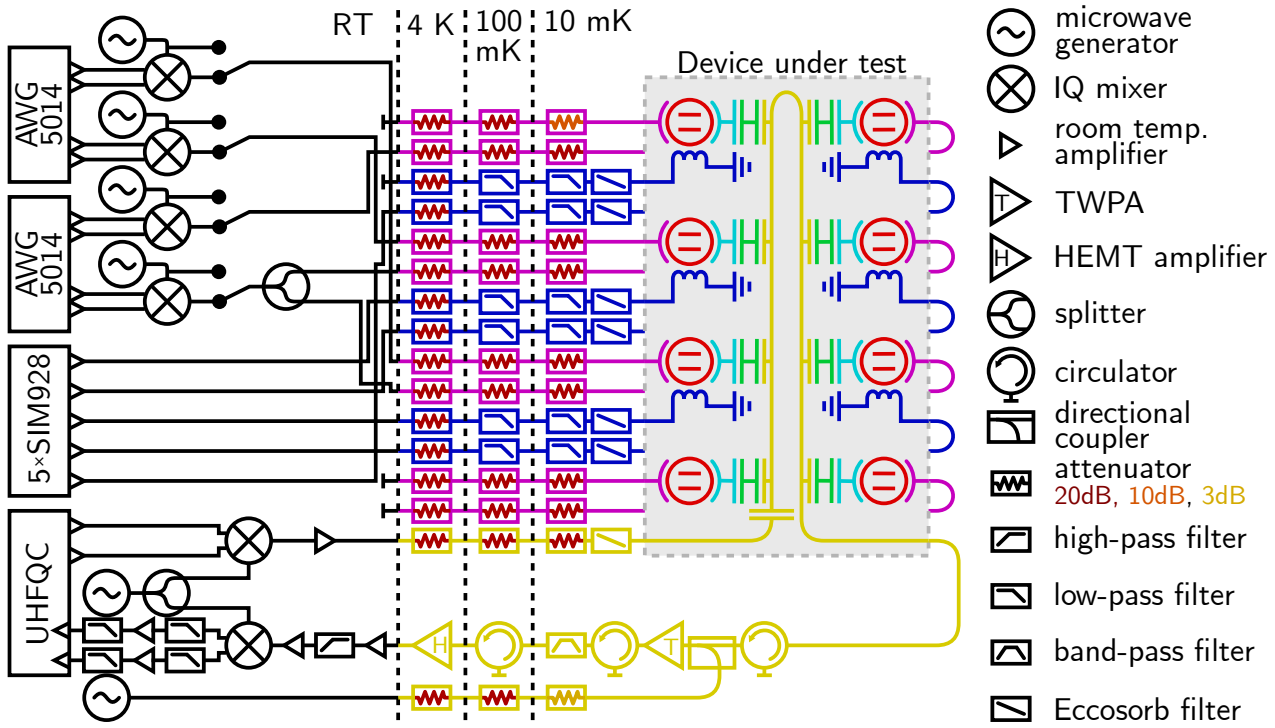

Figure 7: Schematic of the wiring connections

the ground state. The superconducting chip is glued to a printed circuit board (PCB), which is attached to a copper sample holder, mounted to the base plate of the cryostat. We use semi-rigid coaxial cables to connect the PCB to the front-panel of the fridge at room temperature. The input lines are attenuated at different temperature stages to suppress the thermal noise from the room temperature environment. To further shield the device from magnetic field fluctuations, the sample holder is placed in a two-layer magnetic shield can made of Cryoperm.

The cabling diagram is shown in Fig. 7. We use arbitrary waveform generators (AWGs)[1] to generate the baseband quadratures of the qubit drive pulses. These are upconverted using an IQ-mixer to the qubit frequency. To do spectroscopic measurements, we can apply a continuous microwave tone from the microwave generator (MWG)[2], that is normally used as the LO for the upconversion, directly to the qubit drive line, bypassing the mixer with a microwave switch. The flux bias currents are created using SIM928 dc voltage sources from Stanford Research Systems. The instrument can also be used to apply a dc current to a coil below the device to apply a

[1]Tektronix AWG5014
[2]Rohde & Shwarz SGS100A

global magnetic field. The two quadratures of the baseband readout pulse (see Section 2.4) are generated by the Zurich Instruments UHFLI instrument. We are using the special quantum controller (QC) firmware of the UHFLI, so the instrument in this configuration is also called the UHFQC. The baseband quadratures are upconverted using an IQ-mixer. After passing through the half-feedline, the readout tone is amplified by a TWPA [33] at the base temperature, and thereafter by a HEMT at the 4 K stage. Compared to the Josephson parametric amplifier [32], the TWPA has a much wider bandwidth, which allows us to use broadband readout pulses. There are several additional amplifiers at room temperature. Another IQ-mixer, that uses the same LO as the upconversion mixer, is used for downconversion of the readout signal (see Section 2.2). Both the input and output channels of the UHFQC have 600 MHz of bandwidth. Because we are using an IQ-mixer, we can independently choose the signals in the upper and the lower sideband of the upconverted pulse. This means that the readout pulse can have up to 1.2 GHz of bandwidth. This bandwidth limit lead to the frequency spacing of 160 MHz between the readout resonators of the final 8-qubit device M85BM2 described in Section 3.1.

3.3 Signal processing with the UHFQC

The first digital signal processing is done on the UHFQC. An overview of the signal processing capabilities of the UHFQC is shown in Fig. 8. Upon receiving a trigger pulse, timetraces of the two input channels are recorded, which we denote as the real and imaginary part of a complex signal $D[k]$. These timetraces can directly be read out at the so called *input average* node of the UHFQC. In the next step the real and imaginary part of the complex signal can be mixed by a linear transformation

$$\mathrm{Re}\{D[k]\} \to c_{rr}\,\mathrm{Re}\{D[k]\} + c_{ri}\,\mathrm{Im}\{D[k]\} \tag{3.1a}$$

$$\mathrm{Im}\{D[k]\} \to c_{ir}\,\mathrm{Re}\{D[k]\} + c_{ii}\,\mathrm{Im}\{D[k]\} \tag{3.1b}$$

or equivalently

$$D[k] \to \left(\frac{c_{rr}+c_{ii}}{2} + i\frac{c_{ir}-c_{ri}}{2}\right)D[k] + \left(\frac{c_{rr}-c_{ii}}{2} + i\frac{c_{ir}+c_{ri}}{2}\right)D^*[k]. \tag{3.2}$$

The coefficients $c_{rr}, c_{ir}, c_{ri}, c_{ii}$ can be arbitrarily programmed. This transformation is called the *deskew matrix* and can be used to correct for amplitude and phase imperfections of the downconversion mixer (see Section 2.3.2). It is not so useful in the case of multiplexed readout

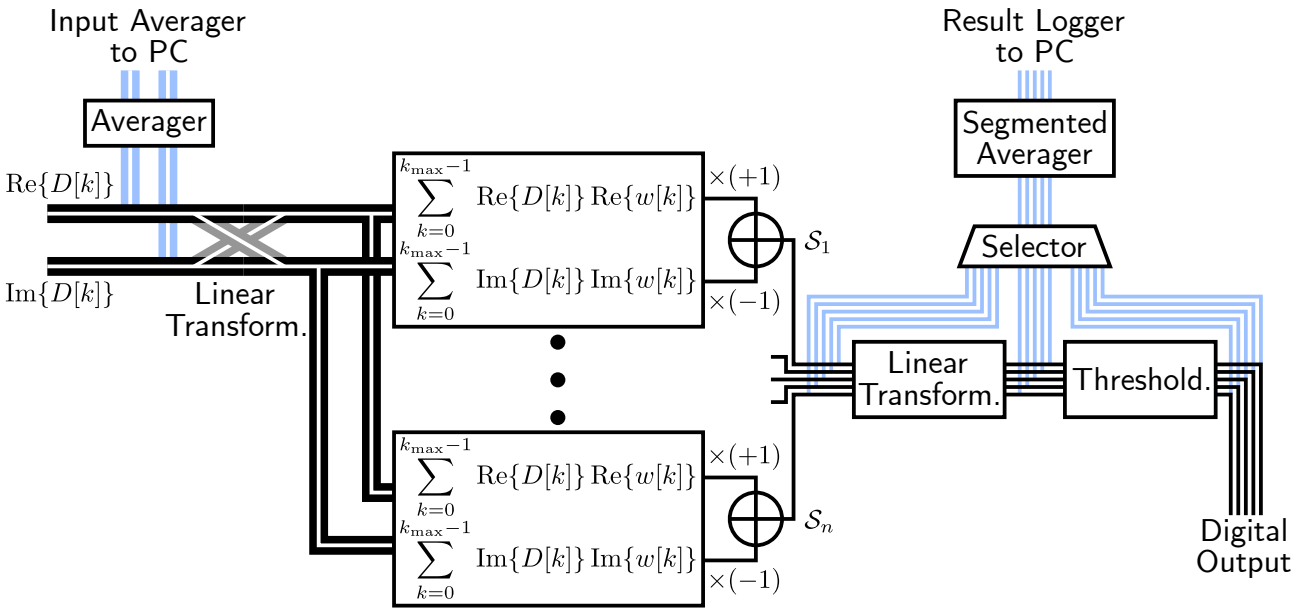

Figure 8: Diagram of the signal processing with the UHFQC

as the phase and amplitude imperfections of the downconversion mixer typically depend on the intermediate frequency and thus cannot be corrected with a global transformation.

The deskewed signal is integrated in the weighted integration units, each programmable with unique integration weights $w[k]$. In the firmware of the UHFQC used in this thesis (v5.2), there were 5 weighted integration units available, but Zurich Instruments has recently released firmware that increases this number to 9. The integration results for the two input channels are then added together in each weighted integration unit with arbitrary weights w_r and w_i to yield the integrated signal $\mathcal{S}$

$$\mathcal{S} = w_r \sum_{k=0}^{k_{\max}-1} \mathrm{Re}\{D[k]\}\,\mathrm{Re}\{w[k]\} + w_i \sum_{k=0}^{k_{\max}-1} \mathrm{Im}\{D[k]\}\,\mathrm{Im}\{w[k]\}, \tag{3.3}$$

which for the choice $w_r = 1$, $w_i = -1$ gives us Eq. (2.26) that we analyzed in Section 2.2.

The integrated signals of each weighted integration unit can be read out or processed further. The processing includes applying a linear transformation to correct for systematic correlations, multiplying the integration results of different weighted integration units and thresholding the integrated results at some preprogrammed level. The output node of the processed or unprocessed integrated signals is called the *result logger*. The thresholded values can also be output to the

digital output port of the UHFQC to condition the following qubit operations on the measurement results in a feed-forward experiment.

Most experiments we do consist of subexperiments, or *segments*, with different configuration parameter values. These subexperiments are usually executed in an interleaved fashion, where consecutive runs of the experiment are saved in different averaging bins, to avoid systematic errors from parameter drifts while averaging the integrated signal in long measurements. This segmented averaging is also colloquially called TV-mode. The UHFQC result logger supports segmented averaging of the integrated signals unlike, the input averager, which can only average the timetraces from a single subexperiment at a time. This means that for each timetrace that one wants to measure with the UHFQC there is the increased overhead associated with setting up the measurement and reading out the results from the UHFQC.

Reading out only the integrated signals differs from what is done in most other setups in our group, where the timetraces are filtered and saved using a custom field-programmable gate array (FPGA) and later analysed on a PC [43]. The filtering on the FPGA includes digital downconversion and a finite impulse response (FIR) filter, both of which are linear operations so that the filtered signal $F[k]$ can be expressed as

$$F[k] = \sum_l \lambda[k,l] D[l], \tag{3.4}$$

where $D[l]$ is the digitized signal. For example for a box-car filter of l_{lmax} samples and digital downconversion from frequency ω_{RO} the coefficients $\lambda[k,l]$ are

$$\lambda[k,l] = \begin{cases} \frac{1}{l_{\mathrm{max}}} e^{i\frac{\omega_{\mathrm{RO}}}{\nu_{\mathrm{S}}} l}, & \text{if } k - l_{\mathrm{max}} < l \leq k, \\ 0 & \text{otherwise.} \end{cases} \tag{3.5}$$

The probabilities P_s of the system being in one of its states s are later calculated on a PC as

$$P_s = \frac{\sum_k \mathrm{Re}\{F[k] R_s[k]^*\}}{\sum_n R_s[n] R_s[n]^*} = \mathrm{Re}\left\{ \sum_l \frac{\sum_k \lambda[k,l] R_s[k]^*}{\sum_n R_s[n] R_s[n]^*} D[l] \right\}, \tag{3.6}$$

where $R_s[k]$ are reference traces recorded after preparing the qubit in the corresponding state. By comparing Eq. (3.6) with Eqs. (2.26) and (3.3) and by identifying the weights as $w[l] = \sum_k \lambda[k,l] R_s[k]^* / \sum_n R_s[n] R_s[n]^*$, we see that the same signal processing can be done on the UHFQC.

4 Tune-up and characterization of multiplexed readout

In this chapter the experimental results are presented. In Section 4.1 we report on the tune-up and characterization experiments necessary prior to implementing multiplexed readout. Example data from measurements on qubit Q6 is shown in the figures while the relevant parameters of all the qubits are shown in table form. The results reported here are from the device M85BM2 used for multiplexed readout experiments, but similar characterization measurements were done on the devices before that to find the features of the design that have to be improved. In Section 4.2 the demonstration and characterization experiments of multiplexed readout are presented.

4.1 Tune-up of single-shot readout

4.1.1 Spectroscopic measurements

The transmission spectrum through the half-feedline, seen in Fig. 9a, shows 8 resonances with a double-dip structure, corresponding to the resonator pairs. The ripples between the resonances are caused by the varying gain of the TWPA and possibly by standing waves in the readout

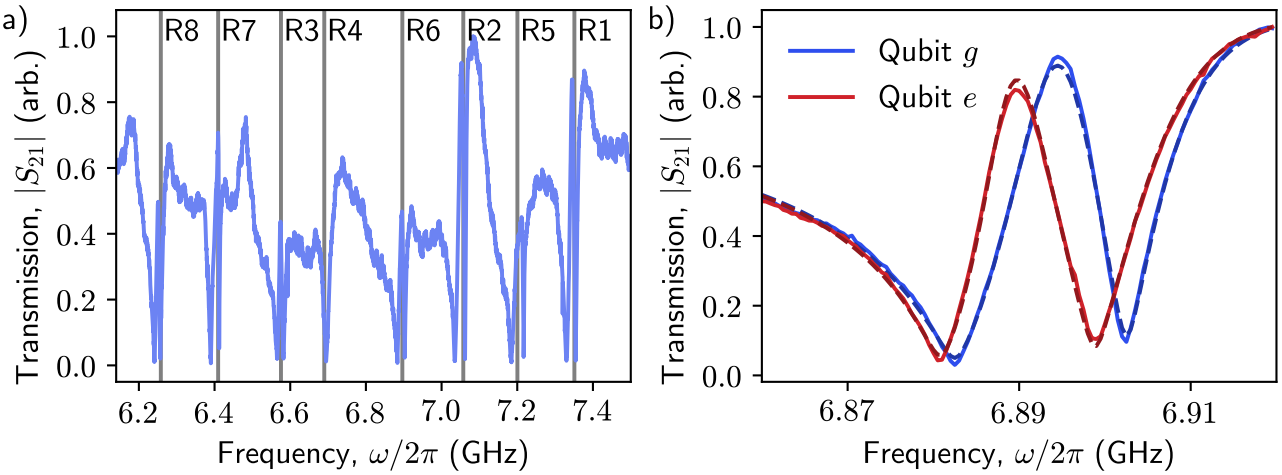

Figure 9: a) The transmission amplitude of the half-feedline with 8 double resonator resonances shown with vertical lines. b) Qubit Q6 state dependent transmission of the half-feedline. Fits to the model (2.78) are shown in dashed lines.

	R2	R3	R5	R6	R7
$\omega_R/2\pi$ (GHz)	7.0534	6.5744	7.1995	6.8947	6.4069
$\omega_P/2\pi$ (GHz)	7.0563	6.5790	7.1962	6.8995	6.3929
$\gamma_R/2\pi$ (MHz)	2.3	1.8	1.0	1.4	1.7
$\kappa_P/2\pi$ (MHz)	32.8	32.1	40.9	33.7	41.7
$J/2\pi$ (MHz)	9.4	8.3	9.9	8.7	7.7
$\chi/2\pi$ (MHz)	-4.0	-1.1	-0.9	-2.7	-2.6
$\kappa_R/2\pi$ (MHz)	8.3	7.7	10.9	7.3	3.3

Table 1: Microwave properties of the 5 readout resonators

chain. By fitting the transmission amplitude around the resonance to the model (2.78), we extract the microwave parameters of the two resonators: the frequencies $\omega_R \pm \chi$ and ω_P, the couplings κ_P and J and the internal loss rate γ_R. To find the dispersive shift χ, we measure the transmission spectra while preparing the qubit in the ground and in the excited state, seen in Fig. 9b. The dispersive shift is given by twice the difference of the fitted readout resonator frequencies (see Eq. (2.5)). The extracted microwave parameters for the 5 resonator pairs we used for multiplexed readout experiments are shown in Table 1. The effective readout resonator linewidth is calculated for the qubit in the excited and ground state from Eq. (2.80) and the smallest of the two values is reported, as the smaller value will limit the speed of populating and depleting the readout resonator in the worst case.

4.1.2 Single qubit gates tune-up

The approximate qubit frequencies are determined in a two-tone qubit-spectroscopy experiment [44]. Here we apply a drive tone with varying frequency to the drive line of the qubit. When the tone is resonant with the qubit frequency, the excited state becomes populated and the transmission through the half-feedline at the corresponding readout resonator frequency changes. By applying an even stronger drive tone, it is also possible to drive the $g \leftrightarrow f$ transition in a two-photon process. From the corresponding drive frequency $\omega_{gf/2} = \omega_Q + \alpha/2$, we extract the anharmonicity α of the qubit.

To rotate the qubit state on the Bloch sphere, we apply a derivative-removal-by-adiabatic-gate

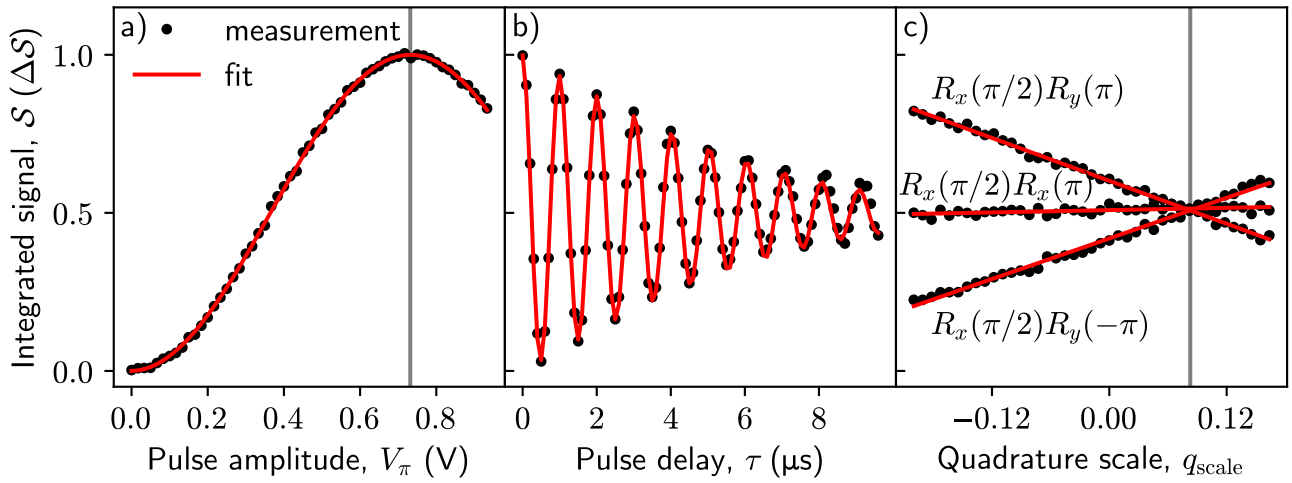

Figure 10: Tune-up of single-qubit gates on the example of qubit Q6. a) The pulse amplitude is swept to find the amplitude corresponding to a π-rotation in the Rabi experiment. b) The detuning between the qubit and drive pulses is given by the frequency of state oscillation between the two $\pi/2$-pulses in the Ramsey experiment. c) In the q-scale experiment the optimal amplitude of the derivative quadrature of the DRAG pulse is found.

(DRAG) [45] pulse to the drive line of the qubit. The DRAG pulse has a Gaussian envelope on one quadrature and the derivative of the Gaussian on the other, designed to correct for phase errors and leakage out of the computational basis due to higher energy levels of the qubit. The standard deviation of the Gaussian is $\sigma = 10\,\text{ns}$ and we truncate it at $\pm 2.5\,\sigma$ to get a total pulse length of 50 ns. The rotation angle is controlled by the pulse amplitude and the rotation axis by its phase. The pulse amplitude corresponding to a rotation of π-radians V_π is calibrated by measuring the oscillations of the integrated signal as a function of the pulse amplitude in the Rabi experiment, shown in Fig. 10a. The data is fitted to a cosine and the π-pulse amplitude is taken to be the maximum of the fit.

The qubit frequency is more precisely determined in a Ramsey experiment, shown in Fig. 10b. We apply two pulses with a varying delay τ between them to the qubit, each rotating the qubit state by $\pi/2$ along the same axis. If the qubit frequency ω_Q is detuned from the frequency of the pulses ω_d, the resulting signal will oscillate with the detuning frequency. Additionally the oscillation amplitude will decay due to dephasing during the experiment:

$$\mathcal{S}(\tau) \propto e^{-\tau/T_2^*} \cos((\omega_\text{Q} - \omega_\text{d})\tau). \tag{4.1}$$

To better distinguish the detuning from decay, we introduce an artificial detuning $\Delta_{\text{art.}}$, such that the rotation axis of the second $\pi/2$-pulse is rotated by $\Delta_{\text{art.}}\tau$. We extract the oscillation frequency of the measured signal $\omega_{\text{Q}} - \omega_{\text{d}} - \Delta_{\text{art.}}$ from a fit.

The higher energy levels of the qubit perturb the driven system such that the effective rotation angle for a short pulse is not along the x-y plane when driving at the qubit frequency determined in the Ramsey experiment. To correct for this effect, we optimize the derivative quadrature $V_{\text{Q}}(t)$ amplitude of the DRAG pulse in the q-scale experiment such that the rotation is around an axis perpendicular to the z-axis on the Bloch sphere. We quantify the amplitude of $V_{\text{Q}}(t)$ in terms of the q_{scale} parameter such that

$$V_{\text{Q}}(t) = q_{\text{scale}}\sigma\frac{\mathrm{d}V_{\text{I}}(t)}{\mathrm{d}t}, \tag{4.2}$$

where $V_{\text{I}}(t)$ is the quadrature of the pulse with the Gaussian envelope. We measure the average qubit populations after applying a $\pi/2$ rotation around the x-axis followed by a π-rotation around the y, x or $-y$-axis for different values of the q_{scale} parameter, shown in Fig. 10c. At the optimal value of the q_{scale} parameter the rotations around the y and $-y$-axis give the same result, while at other values, the rotation axis are tilted from what we expect and there is a difference between the $R_y(\pi)$ and $R_y(-\pi)$ rotation.

The qubit frequency and other parameters described in this section depend on the bias magnetic flux through the SQUID loop. The maximum qubit frequency $\omega_{\text{Q,max}}$ is determined in a repeated qubit-spectroscopy experiment while sweeping the flux bias current. The values reported in Table 2 correspond to the flux biasing of the qubits as in the multiplexed readout experiment. All qubits except for Q5 were biased close to their maximum frequency, which means that they are less sensitive to the noise in the biasing magnetic flux. We could not tune qubit Q5 to its maximum frequency because it would quickly decay there due to spontaneous emission through the readout resonator at the small detuning from the readout resonator.

4.1.3 Readout parameters tune-up

We apply a square pulse A_{in}, modulated at the the readout frequency ω_{RO}, at the input of the fridge to determine the state of a single qubit. To pick the optimal modulation frequency ω_{RO} (also called readout frequency), we measure the complex transmission of the half-feedline for the qubit in the excited state $S_{21}^{e}(\omega)$ and for the qubit in the ground state $S_{21}^{g}(\omega)$. We

	Q2	Q3	Q5	Q6	Q7
$\omega_{\mathrm{Q,max}}/2\pi$ (GHz)	6.260	5.216	6.996	5.996	5.442
$\omega_{\mathrm{Q}}/2\pi$ (GHz)	6.2600	5.2157	5.449	5.9178	5.4421
$\alpha/2\pi$ (MHz)	−226	−246	−198	−234	−238
V_π (mV)	191	203	550	730	458
q_{scale} (%)	5.9	4.3	8.3	8.3	0.2
T_2^* (µs)	3.4	10	0.6	7.5	6.5

Table 2: Properties of the 5 qubits used in the multiplexed readout experiment.

choose the frequency where the absolute value of the difference of the transmission amplitudes is maximal, so that the SNR in the steady state, as given by Eq. (2.31), is maximized. The measured transmission amplitudes and their difference for qubit Q6 is shown in Fig. 11. The readout frequencies ω_{RO} of the other 4 qubits reported in Table 3 are picked in the same way.

To pick the optimal readout amplitude for a given pulse length a balance between low SNR at low readout amplitudes and breakdown of the dispersive approximation and qubit state mixing at high readout amplitudes must be found. We chose a readout pulse length of 80 ns as it enabled

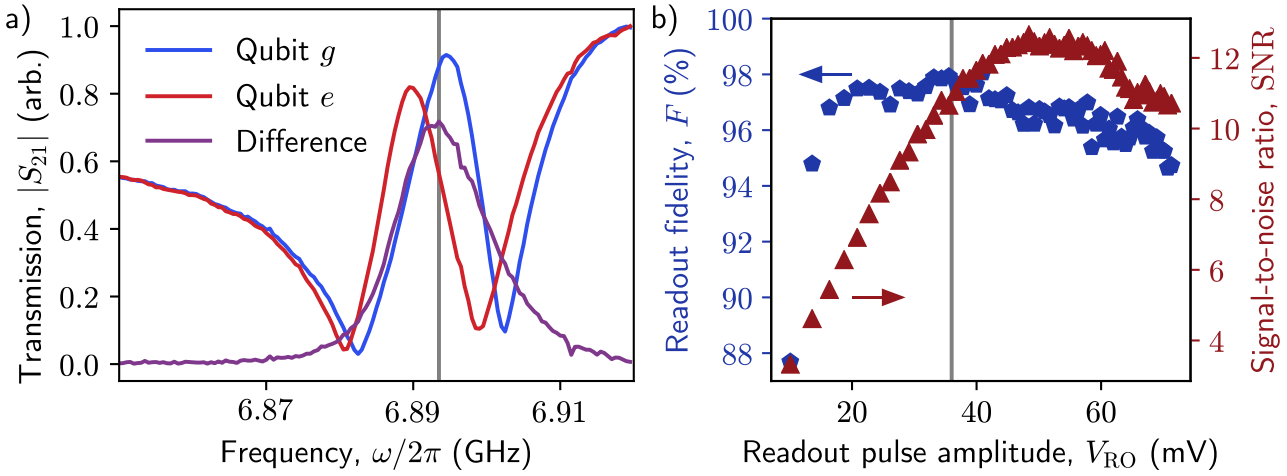

Figure 11: a) The readout frequency of qubit Q6 is set to $\omega_{\mathrm{RO}}/2\pi = 6.8935\,\mathrm{GHz}$, where the difference between the complex transmission amplitudes between the qubit in the ground- and excited states is maximal. b) The readout pulse amplitude of Q6 was chosen $V_{\mathrm{RO}} = 36\,\mathrm{mV}$ such that the readout fidelity is maximized for the chosen pulse length and frequency.

us to accumulate enough SNR to reliably distinguish between the two states while keeping the number of photons in the readout resonator n_{RO} in the order of the critical photon number $n_{\mathrm{crit.}}$. The readout amplitude was chosen for each qubit by sweeping the readout amplitude while recording the probability distributions $p(\mathcal{S} \mid 0)$ and $p(\mathcal{S} \mid \pi)$. These distributions for qubit Q6 at the readout amplitude used for multiplexed readout are shown in Fig. 12. Each of the measurement results is classified as the qubit being in the ground or excited state according to the threshold value, shown with the dashed line. The fidelity of the readout F was calculated for each amplitude according to Eq. (2.60). To extract the signal-to-noise ratio, a double-Gaussian was fitted to both distributions and the SNR calculated as

$$\mathrm{SNR} = \frac{\mu^e - \mu^g}{(\sigma_e + \sigma_g)/2}, \tag{4.3}$$

where $\mu^{e/g}$ and $\sigma^{e/g}$ are the mean and the standard deviation of the corresponding Gaussian. The extracted fidelity and SNR for reading out qubit Q6 are plotted as a function of the readout amplitude in Fig. 11b. For each qubit we choose the readout amplitude where the total fidelity is maximal. The loss of fidelity due to low SNR is given by the *overlap error*

$$\varepsilon_{\mathrm{o}} = \mathrm{erfc}\left(\frac{\mathrm{SNR}}{2\sqrt{2}}\right). \tag{4.4}$$

At the readout amplitude we chose for qubit Q6, the overlap error is $\varepsilon_{\mathrm{o}} \ll 10^{-5}\,\%$ and the errors are mainly due to state transitions during or before the measurement.

To determine the number of photons in the readout resonator corresponding to the selected readout amplitude, we do an ac-Stark shift measurement. From the dispersive Hamiltonian Eq. (2.5) we see that the effective qubit frequency depends on the number of photons in the readout resonator. We apply a readout pulses of 3.192 µs with different amplitudes V, expressed in terms of the ratio to the amplitude used in single-shot readout experiments $V = \xi V_{\mathrm{RO}}$. At the same time, we apply a drive pulse a frequency ω_{d} near the qubit transition frequency. We integrate the last 2.275 µs of the transmitted readout pulse to determine the qubit state. The signal as a function of the drive frequency is fitted to a Lorentzian function and the qubit frequency ω_{Q} and linewidth are extracted as the mean and full width at half maximum (FWHM) of the fit. Example data for qubit Q6 at $\xi^2 = 0.9\,\%$ is seen in Fig. 13a. Repeating this measurement at different readout amplitudes, we find the qubit frequency as a function of the scale parameter. We fit the data to the model $\omega_{\mathrm{Q}} = \omega_{\mathrm{Q},0} + 2\chi n_{\mathrm{RO}}\xi^2$ of the dispersive Hamiltonian Eq. (2.5), where $\omega_{\mathrm{Q},0}$ and $2\chi n_{\mathrm{RO}}$ are the fit parameters. Finally, we can calculate the number of photons

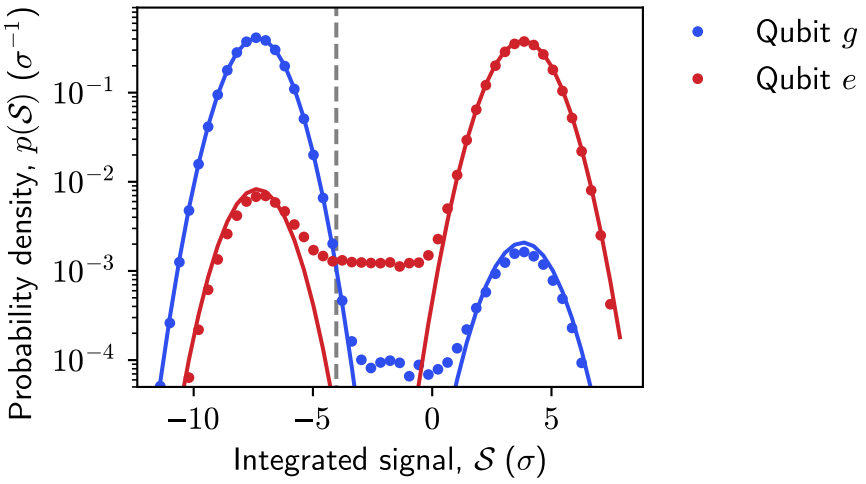

Figure 12: Histograms of the integrated signal results of reading out qubit Q6. The qubit was prepared in the ground state for the histogram in blue, and in the excited state for the histogram in red. The experimental results are shown as circles while a fit to a double-Gaussian model is shown with lines. The two peaks are well separated, which means that a smaller readout amplitude could have been used.

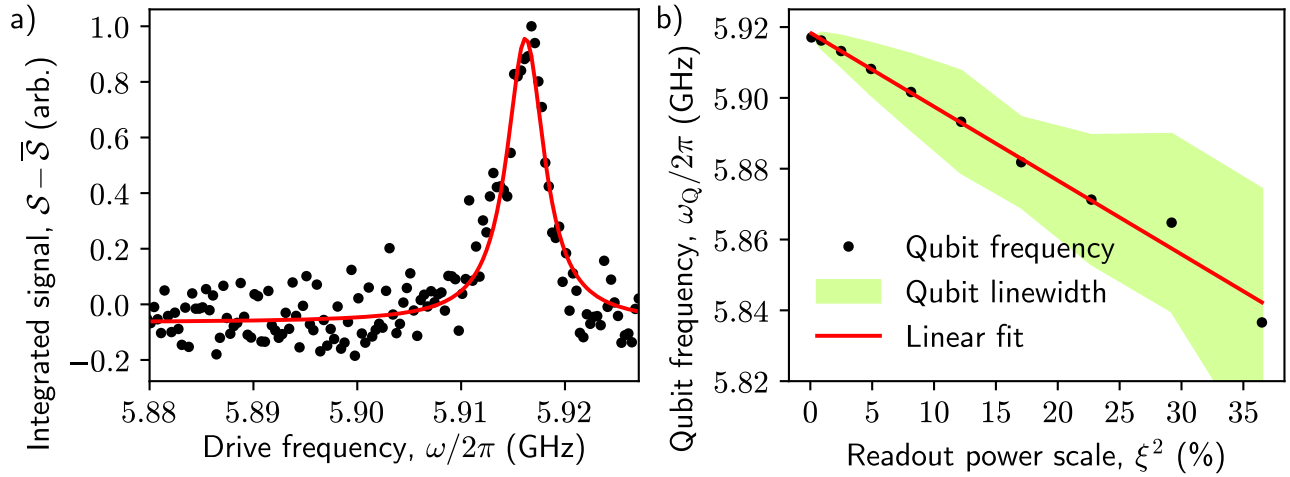

Figure 13: a) The frequency of the qubit drive tone is swept, recording the transmitted signal. We see a change in the transmitted signal when the qubit drive tone is resonant with the qubit transition frequency. The qubit frequency and linewidth are extracted from a Lorentzian fit. b) Repeating the qubit spectroscopy measurement at different readout amplitudes we see a linear dependence between the qubit frequency and readout power. The number of photons in the readout resonator at $100\,\%$ is extracted from a linear fit.

	Q2	Q3	Q5	Q6	Q7
$\omega_{\mathrm{RO}}/2\pi$ (GHz)	7.0535	6.5720	7.2013	6.8935	6.4080
$(\omega_{\mathrm{RO}} - \omega_{\mathrm{LO}})/2\pi$ (MHz)	192.5	−289.0	340.3	32.5	−453.0
$(\omega_{\mathrm{RO}} - \omega_{\mathrm{Q}})/2\pi$ (MHz)	793.5	1356.3	1752.3	975.7	965.9
V_{RO} (mV)	8.625	30.75	57.0	36.0	29.25
n_{RO}	4.7	36.3	126.8	39.2	56.2
$n_{\mathrm{crit.}}$	9.5	33.9	42.2	16.1	18.7

Table 3: Readout parameters of the 5 qubits used in the multiplexed readout experiment.

in the readout resonator for $\xi = 100\,\%$, n_{RO}, by using the value of the dispersive shift χ from an independent measurement (see Fig. 9b).

4.1.4 Mode-matched filtering

To extract the most SNR from the digitized signal, we use mode-matched integration weights in single-shot readout experiments. As derived in Subsection 2.3.1, they give the highest possible SNR. For this we record the averaged traces for the qubit in the ground excited state and use the complex conjugate of their difference as the integration weight. The timetraces are averaged 2^{15} times giving a filter efficiency $\eta_{\mathrm{f}} > 99.9\,\%$ according to Eq. (2.42). This efficiency is actually not achieved, as we are not correcting for the phase and amplitude imbalance of the downconversion mixer as per Eq. (2.51b). The downconverted signal for qubit Q6 in the ground and excited state together with their difference is shown in Fig. 14. The oscillation at $2\omega_{\mathrm{IF}}/2\pi = 65\,\mathrm{MHz}$ in the difference of the downconverted signals comes from the downconversion mixer imperfections. In comparison, the maximal filter efficiency achievable with a box-car filter is $\eta_{\mathrm{f}} = 89\,\%$, when integrating from 47.8 ns to 161.7 ns. If not optimizing the filter at all and choosing a box-car weight starting at the arrival of the pulse and ending at $\tau_{\mathrm{p}} + \frac{1}{\kappa_{\mathrm{R}}} = 217\,\mathrm{ns}$, the resulting efficiency would be $\eta_{\mathrm{f}} = 60\,\%$.

We pick the local oscillator frequency, which is common for all of the qubits, such that the overlap between the weight spectra of different qubits is minimized to reduce signal crosstalk. Due to constraints of the UHFQC, the integration weights are normalized such that $\max_k(\mathrm{Re}\{w[k]\}, \mathrm{Im}\{w[k]\}) \leq 1$. In Fig. 15b, we see that the peaks are well separated

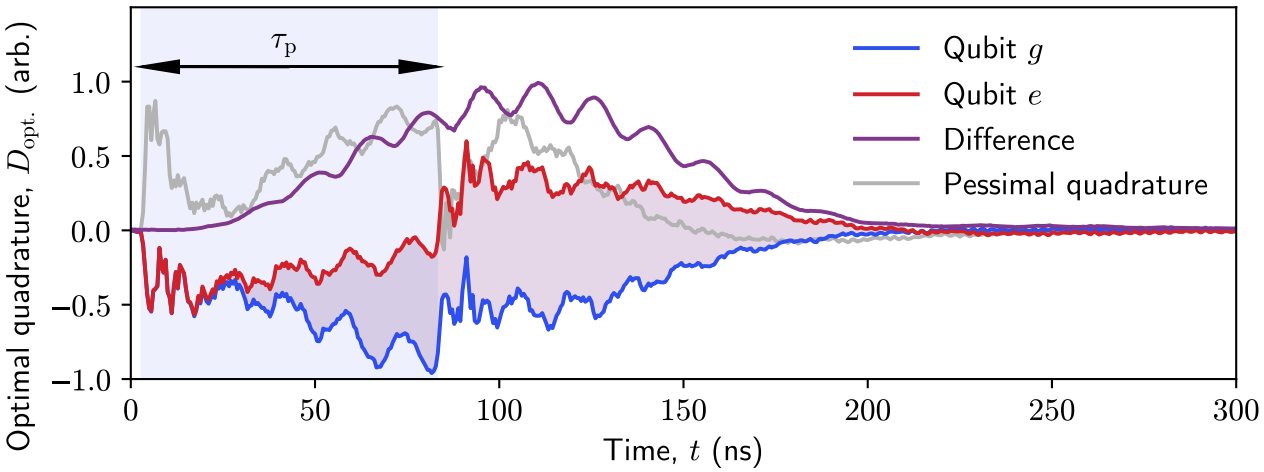

Figure 14: The measured responses to the $\tau_p = 80\,\text{ns}$ readout pulse of qubit Q6 for the qubit in the ground and excited states. The digitally downconverted quadrature that shows the largest difference between the two traces is plotted. The absolute value of the difference of the two responses, which is used as the mode-matched integration weight, is shown in purple. The quadrature orthogonal to the optimal quadrature, averaged over the two states, is shown in gray.

in frequency with 5 orders of magnitude suppression in power at neighbouring qubit readout frequencies. The input pulse powers, shown in Fig. 15a, are however suppressed only by 3 orders of magnitude at the neighbouring qubit readout frequencies.

4.1.5 Timing

In some experiments the exact relative arrival time of the pulses generated by different instruments is important. To characterize the delays between the AWGs and the UHFQC, we generated a 10 ns pulse from each of these instruments, let it propagate through the cryostat and the device, and measured the arrival time of using the UHFQC. In Fig. 16a we see the pulse generated by the UHFQC and acquired by the UHFQC with the same physical trigger starting both events. From this measurement we find the optimal delay value of 216 ns between UHFQC pulse generation and data acquisition. In Fig. 16b a trigger for the UHFQC and a pulse to the drive line of qubit Q2 are generated using one of the AWGs. The modulation frequency of the drive pulse is resonant with R2 and the output from the half-feedline is measured by the UHFQC. We see that if we want the pulses to arrive at the sample simultaneously, we need to advance the UHFQC

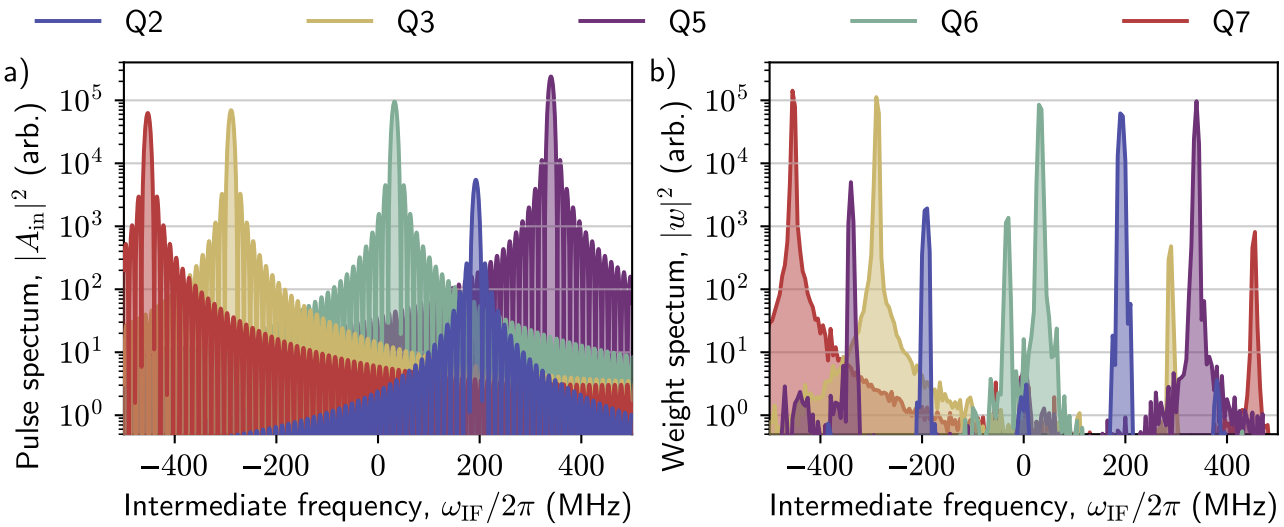

Figure 15: a) The power spectra of the readout pulses of the individual qubits, calculated from the drive parameters. b) Power spectra of the mode-matched integration weights.

trigger by 176 ns. The delay between pulses from the master AWG and the slave AWG (the master AWG triggers the slave AWG) and between the gate pulse to mask the qubit drive tone from a MWG and the readout pulse were calibrated in the same way, yielding the values 414 ns and 62 ns correspondingly.

4.2 Characterization of multiplexed readout

4.2.1 Assignment probability table

After finding the optimal parameters of single-qubit gates, necessary for state preparation, and optimizing the readout amplitude, frequency and weight functions, we are ready for demonstrating multiplexed readout. For this we prepare one of the 32 computational basis states of the 5 qubit system and apply the five-tone measurement pulse to the half-feedline. We record 2 064 384 shots for each of the prepared states. The qubits are not always in the ground state at the start of the experiment due to thermal population. To filter out the shots, where some of the qubits are initially in the excited state, we also do a preselection measurement 400 ns before the main measurement. Later, while analysing the data, we discard the shots where not all of the qubits were initially in the ground state. In the multiplexed readout dataset, this amounts to 30.8 %

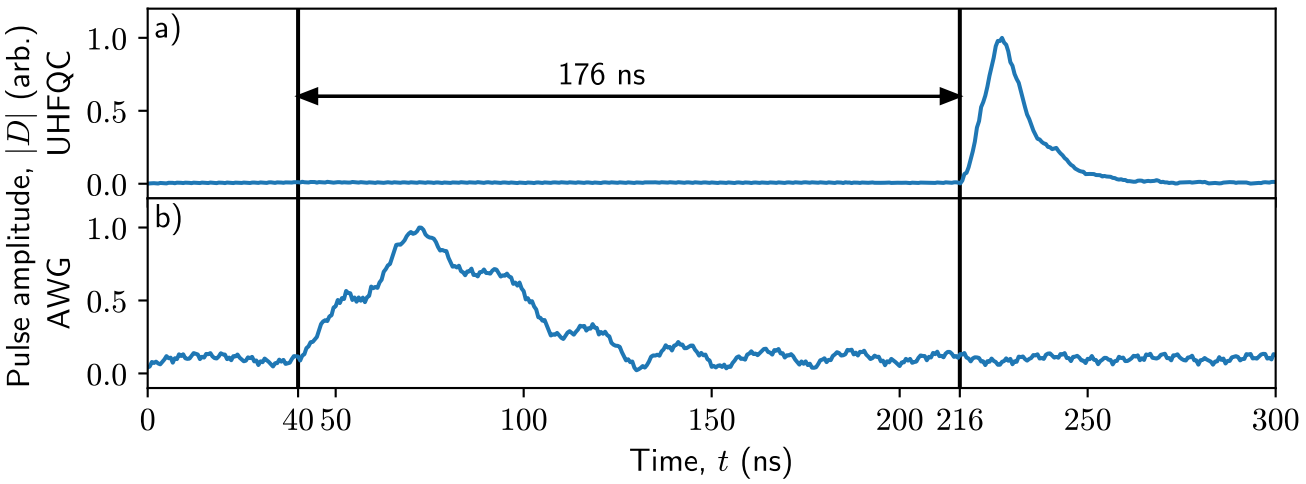

Figure 16: Calibration of the delays between the readout and the drive pulses. a) The UHFQC is used to generate a $10\,\mathrm{ns}$ square pulse. The acquired time-trace shows that it arrives back at the UHFQC $216\,\mathrm{ns}$ after the start of data acquisition. The frequency of the pulse is chosen between the resonances so that it passes through the half-feedline relatively unperturbed. b) A $10\,\mathrm{ns}$ square pulse is generated using the AWG. The pulse frequency is chosen to be in resonance with resonator R2 to see any transmission to the output port of the half-feedline. The frequency dependence of the resonator structure distorts the pulse shape and the signal amplitude oscillates due to LO leakage as the up- and downconversion mixers had different LO frequencies. To downconvert the signals and smooth out noise, the digitized time-traces are convolved with a decaying exponential in both cases, with time-constant $\tau = 7.4\,\mathrm{ns}$. Because of the sharp rise of the used convolution kernel, the convolution does not change the starting times of the pulses.

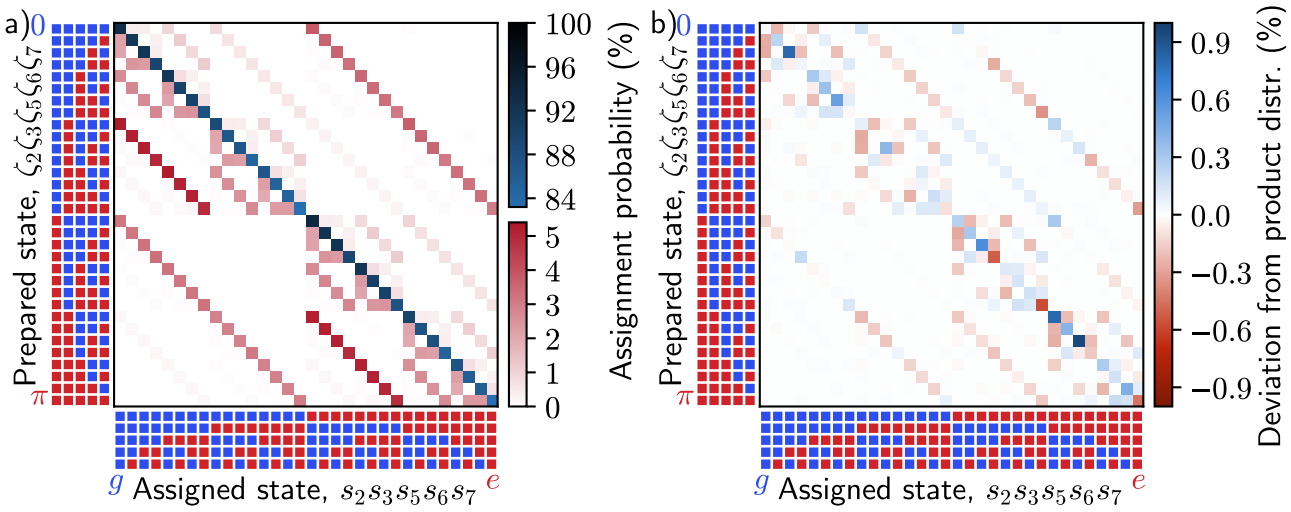

Figure 17: a) Assignment probability of the different 5-qubit states as a function of the prepared state. b) Deviation of the assignment probabilities from a fully separable probability matrix in percentage points.

of the whole dataset. This number is consistent with the excited level populations seen in the individual qubit readout experiments that were done interleaved with the multiplexed readout experiment. There we removed 2.7 %, 6.8 %, 13.4 %, 7.6 % and 7.4 % of the data for qubits Q2, Q3, Q5, Q6 and Q7 respectively. For each qubit Qi we first analyse the distributions $p(\mathcal{S}_i \mid 0_i)$ and $p(\mathcal{S}_i \mid \pi_i)$ averaged over the different preparations of the other 4 qubits to find the threshold voltage $\mathcal{S}_{0,q}$. Using these thresholds, we can label the measurement results with one of the 32 states of the 5 qubits. The resulting assignment probability matrix $P(s_2s_3s_5s_6s_7 \mid \zeta_2\zeta_3\zeta_5\zeta_6\zeta_7)$ is shown in Fig. 17a.

In the ideal case the diagonal elements would all be 100 % while the off-diagonals would be 0 %. The apparent deviation from the ideal corresponds mainly to errors in classification of a single qubit. To better visualize any correlations in the probabilities, we calculate the average probability table $P(s_q \mid \zeta_q)$ for each qubit and find their Kronecker product as described in Subsection 2.4.1. The resulting matrix does not have any correlations between the measurement results of the qubits. The deviation of the original probability matrix from the product of the individual matrices is shown in Fig. 17b. The difference is less than 1 percentage point for all elements. It is not entirely clear what limits this type of crosstalk, but possible reasons include environment-induced crosstalk, as significant fluctuations average single qubit readout fidelities were witnessed

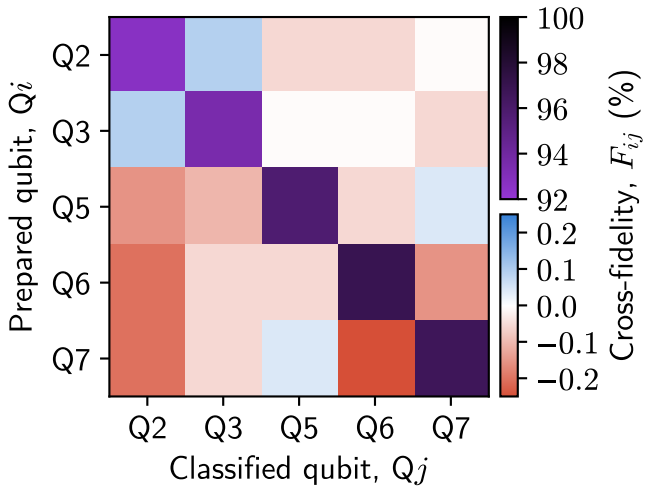

Figure 18: The cross-fidelity matrix, quantifying the correlations between the preparation of qubit Qi and the measurement result of qubit Qj.

	Q2	Q3	Q5	Q6	Q7
$F^{(1)}$ (%)	91.4	93.1	95.4	97.5	96.9
$F^{(5)}$ (%)	92.7	93.5	95.7	97.0	96.6

Table 4: Readout fidelity of individual readout $F^{(1)}$ and average readout fidelity in multiplexed readout $F^{(5)}$ of the 5 qubits.

during the 13 hour data acquisition time.

From the assignment probability matrix we also calculated the cross-fidelity matrix F_{ij}, given by Eq. (2.62) and shown in Fig. 18. The diagonal elements, which give the average single qubit readout fidelity, are greater than 92 % for all 5 qubits, while the off-diagonal elements are all less than 0.23 %. The average readout fidelities in the multiplexed readout experiment $F^{(5)}$ match well with the readout fidelities obtained from the experiments where only one qubit was read out at a time $F^{(1)}$, as seen in Table 4.

4.2.2 Cross-measurement induced dephasing

So far we have looked at how the preparation of the 5 qubits affects the measurement results of the same 5 qubits. There are many scenarios, for example linear error correcting code and

entanglement swapping algorithm, where not all qubits connected to the half-feedline are read out at the same time. The effect of measurement on the unmeasured qubits can be characterized, as described in Section 2.4, in terms of the dephasing of qubit $\mathsf{Q}j$ caused by the measurement of qubit $\mathsf{Q}i$. To measure this, we conduct a Ramsey dephasing measurement, depicted in Fig. 19. We apply two $\pi/2$-pulses on the dephased qubit $\mathsf{Q}j$, with a variable phase difference ϕ. Between the two $\pi/2$-pulses, we apply a measurement pulse with varying amplitude to qubit $\mathsf{Q}i$. As when determining the number of photons in the readout resonator, we quantify the amplitude of the pulse V with the ratio ξ to the one used in the multiplexed readout experiment $V = \xi V_{\mathrm{RO}}$. There is a delay of 420 ns after the measurement pulse to also be sensitive to dephasing while the resonator is ringing down. After the second $\pi/2$-pulse we measure the state of qubit $\mathsf{Q}j$.

For each readout amplitude ξ, we fit the integrated readout signal $\mathcal{S}$ to a sinusoid as a function of ϕ and extract the contrast C:

$$\mathcal{S}(\xi, \phi) = C(\xi)\cos(\phi + \phi_0(\xi)). \tag{4.5}$$

The extracted contrasts for qubit pair $\mathsf{Q}i = \mathsf{Q}3$, $\mathsf{Q}j = \mathsf{Q}7$ are shown in Fig. 19b. The instantaneous dephasing rate is given by [46]

$$\frac{\mathrm{d}\Gamma}{\mathrm{d}t} = 2\chi\,\mathrm{Im}\{a_{\mathrm{R}}^{g} a_{\mathrm{R}}^{e*}\}, \tag{4.6}$$

where a_{R}^{g} and a_{R}^{e} are the amplitudes of the field in the readout readout resonator for the qubit in the ground and excited states. We note that the dephasing rate, and therefore also the integrated dephasing, are proportional to the power of the readout tone. Therefore we fit the signal contrast to the model

$$C(\xi) = C_0 e^{-\Gamma} = C_0 e^{-\frac{\xi^2}{2\sigma^2}}. \tag{4.7}$$

The integrated dephasing of qubit $\mathsf{Q}j$ due to the measurement of qubit $\mathsf{Q}i$ at $\xi = 100\,\%$ is therefore given by $\Gamma = \frac{1}{2\sigma^2}$.

The dephasing is extracted in this way for all qubit pairs $\mathsf{Q}i$, $\mathsf{Q}j$ and shown in Fig. 19c. The probability of phase flip error on the qubit is given by $P_{\phi\mathrm{e}} = \frac{1}{2}\left(1 - e^{-\Gamma}\right)$ with the worst case value of 50 %. For qubit pairs $(\mathsf{Q}i, \mathsf{Q}j) = (\mathsf{Q}2, \mathsf{Q}3), (\mathsf{Q}2, \mathsf{Q}5), (\mathsf{Q}2, \mathsf{Q}7), (\mathsf{Q}6, \mathsf{Q}3)$ and $(\mathsf{Q}6, \mathsf{Q}7)$, the change in contrast was below the noise level. In these cases we estimated the upper bound of the dephasing Γ by assuming that the contrast changes by one standard deviation of the measured contrasts over the amplitude range considered.

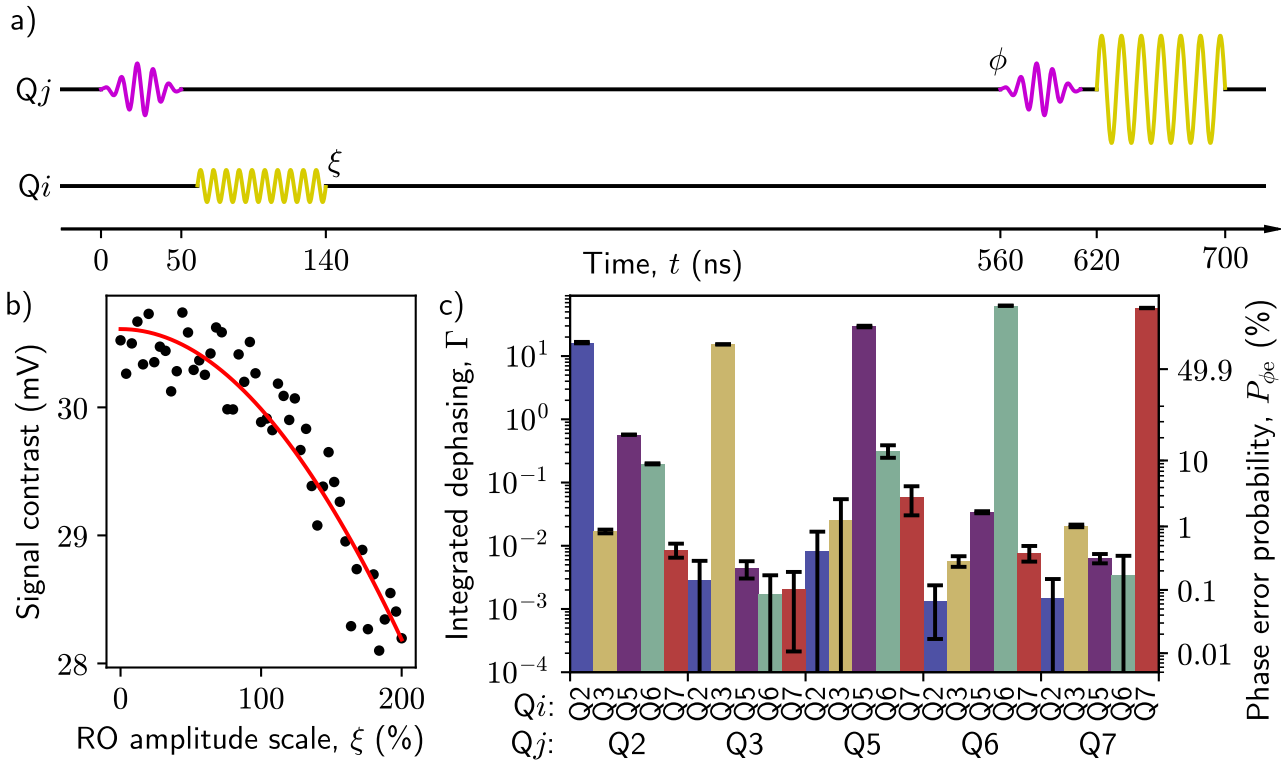

Figure 19: Determining the dephasing of qubit Qj due the measurement of qubit Qi. a) Pulse scheme used for the experiment. A measurement pulse with amplitude $V = \xi V_{\mathrm{RO}}$ is applied to qubit Qi between two $\pi/2$-pulses on qubit Qj with a phase difference of ϕ. Finally the state of qubit Qj is measured. The experiment is repeated at different values of ξ and φ. b) For each amplitude scale ξ, the amplitude of the oscillations of the qubit Qi measurement signal as a function of ϕ is found. Here the experimental data for Qi = Q3, Qj = Q7 is shown together with a fit to a Gaussian. The total dephasing of qubit Qj due to the readout of qubit Qi at the full readout amplitude $\xi = 100\,\%$ is calculated from the fit parameters. c) The integrated dephasing rates of all qubit pairs together with the corresponding probabilities of inducing a phase flip error.

For most qubits the error probability is in the percent order, but the higher dephasing rates of qubit Q2, when measuring the other qubits, can be seen as the result of the high effective linewidth κ_{R} and dispersive shift χ of Q2 (see Table 1). The large linewidth increases the populations a_{R}^{g}, a_{R}^{e} when driving off-resonantly and the high dispersive shift χ directly increases the dephasing according to Eq. (4.6). As a combination of biasing qubit Q5 1.5 GHz from its maximum frequency and a fluctuating magnetic field noise, the measurements of the dephasing of qubit Q5 were not very reliable. The large apparent dephasing rates of qubit Q5 when reading out qubits Q6 and Q7 could thus be explained by fluctuations of its spontaneous dephasing rate during the experiment.

4.2.3 Measurement efficiency

The diagonal elements $\mathsf{Q}i = \mathsf{Q}j$ of the dephasing matrix Fig. 19c enable us to measure the total measurement efficiency η when reading out the qubits [37]. To see this we derive the fundamental relation between the dephasing of the qubit and the achieved SNR in the ideal case. For a linear measurement in the computation basis, the measurement operator has the form

$$\hat{M}(\mathcal{S}) = \frac{1}{\sqrt{\sigma\sqrt{2\pi}}} \begin{pmatrix} e^{-\frac{(\mathcal{S}-\mathcal{S}_g)^2}{4\sigma^2}} & 0 \\ 0 & e^{-\frac{(\mathcal{S}-\mathcal{S}_e)^2}{4\sigma^2}} \end{pmatrix}, \tag{4.8}$$

where σ is noise in the measured signal $\mathcal{S}$, ideally only due to the amplified quantum fluctuations of readout resonator field. This measurement operator is properly normalized with respect to the measurement result $\mathcal{S}$:

$$\int_{-\infty}^{\infty} \hat{M}^{\dagger}(\mathcal{S})\hat{M}(\mathcal{S})\mathrm{d}\mathcal{S} = \begin{pmatrix} 1 & 0 \\ 0 & 1 \end{pmatrix}, \tag{4.9}$$

and gives the following distributions for the qubit prepared in the ground and excited state:

$$p(\mathcal{S} \mid g) = \mathrm{tr}\left(\hat{M}(\mathcal{S})\hat{\rho}_g\hat{M}^{\dagger}(\mathcal{S})\right) = \frac{1}{\sigma\sqrt{2\pi}} e^{-\frac{(\mathcal{S}-\mathcal{S}_g)^2}{2\sigma^2}} \tag{4.10}$$

$$p(\mathcal{S} \mid e) = \mathrm{tr}\left(\hat{M}(\mathcal{S})\hat{\rho}_e\hat{M}^{\dagger}(\mathcal{S})\right) = \frac{1}{\sigma\sqrt{2\pi}} e^{-\frac{(\mathcal{S}-\mathcal{S}_e)^2}{2\sigma^2}} \tag{4.11}$$

with the quantum limited SNR

$$\mathrm{SNR}_{\mathrm{q.l.}} = \frac{\mathcal{S}_e - \mathcal{S}_g}{\sigma}. \tag{4.12}$$

	Q2	Q3	Q5	Q6	Q7
Γ	16.3	15.3	29.3	62.6	57.6
SNR	5.8	5.5	7.1	11.3	10.5
η (%)	51.8	49.9	42.7	51.2	47.9

Table 5: Measurement efficiencies.

With our definition of the measurement efficiency, the actual achieved SNR is given by

$$\mathrm{SNR}^2 = \frac{\eta}{2}\mathrm{SNR}^2_{\mathrm{q.l.}}, \tag{4.13}$$

because we are using a phase preserving amplifier instead of a phase sensitive one, which results in a two-fold reduction of SNR^2. Applying this measurement to a qubit in an arbitrary state $\hat{\rho}_{\mathrm{i}} = \begin{pmatrix} \rho_{gg} & \rho_{ge} \\ \rho_{eg} & \rho_{ee} \end{pmatrix}$ the post-measurement state $\hat{\rho}_{\mathrm{f}}$, averaged over all possible measurement outcomes is

$$\hat{\rho}_{\mathrm{f}} = \int_{-\infty}^{\infty} \hat{M}(\mathcal{S})\hat{\rho}_{\mathrm{i}}\hat{M}^{\dagger}(\mathcal{S})\mathrm{d}\mathcal{S} = \begin{pmatrix} \rho_{gg} & e^{-\frac{(\mathcal{S}_e-\mathcal{S}_g)^2}{8\sigma^2}}\rho_{ge} \\ e^{-\frac{(\mathcal{S}_e-\mathcal{S}_g)^2}{8\sigma^2}}\rho_{eg} & \rho_{ee} \end{pmatrix} = \begin{pmatrix} \rho_{gg} & e^{-\Gamma}\rho_{ge} \\ e^{-\Gamma}\rho_{eg} & \rho_{ee} \end{pmatrix}. \tag{4.14}$$

Using the expression for the integrated dephasing from Eq. (4.14), we arrive at the expression for the measurement efficiency

$$\eta = 2\frac{\mathrm{SNR}^2}{\mathrm{SNR}^2_{\mathrm{q.l.}}} = \frac{\mathrm{SNR}^2}{4\Gamma}. \tag{4.15}$$

Using Eq. (4.15) together with the measurement induced dephasing data from Fig. 19c and the achieved SNR in single-shot readout, we calculate the measurement efficiencies for the 5 qubits, reported in Table 5.

5 Summary & outlook

We implemented multiplexed readout of 5 superconducting qubits using the Zurich Instruments UHFLI instrument and, as the first team in Quantum Device Lab, the PycQED measurement control software package. By employing mode-matched weighted integration, we achieve 92–97 % readout fidelities with a 80 ns readout pulse. The multiplexed readout fidelities differ from the individual readout fidelities of the qubits by less than 1.3 % for all and by less than 0.5 % for most qubits. The 5-qubit state assignment probabilities deviate less than 1 % from the assignment probability distributions of independent qubit, rendering the correlated errors insignificant compared to single qubit errors. The cross-fidelity, indicating the correlations between the measurement result of one and the preparation of an other qubit, is less than 0.23 % for all qubit pairs. The effect of the readout pulse on unmeasured qubits is characterized in terms of cross-measurement induced dephasing. The dephasing induced phase error probabilities are for most qubits in the percent order or less and are limited by the spectral width of the drive pulses.

Zurich Instruments have by now updated the firmware of the UHFQC to support 9 weighted integration units. After fabricating a copy of the current device with all qubits' maximum frequencies near the design values, we could demonstrate the multiplexed readout of 8 qubits. To reduce the amount of cross-dephasing, we also plan to use shaped readout pulses that have a smaller frequency bandwidth for a pulse of the same duration. This would allow us to demonstrate the suppression of off-resonant driving of the readout resonators due to the individual Purcell filters. When in addition to multiplexed readout we have implemented high-fidelity two-qubit gates, an device with 8 linearly coupled qubits could be used to implement a linear error correcting code [47] or an entanglement swapping experiment.

Acknowledgements

I would like to thank my supervisors, Johannes Heinsoo and Christian Kraglund Andersen, who taught me a lot about the experimental and theoretical aspects of quantum physics. They always found time to provide assistance with any questions I turned to them with. I am also very thankful to professor Andreas Wallraff for leading the Quantum Device Laboratory at the forefront of quantum science and creating the opportunity for doing a master's thesis in such an interesting field. The guidance of Christopher Eichler on moving on with the project was also very valuable. I had an interesting time and interesting discussions with the rest of the Quantum Computing team – Sebastian Krinner, Jonas Butscher, Simon Storz and Stefania Balasiu. For their efforts in fabricating the devices used in this project, my thanks go to Theo Walter, Simone Gasperinetti, Jean-Claude Besse and Anton Potocnik. I thank Theo Walter for his previous work and instructions on single qubit readout. I also thank all the rest of the QuDev members who I have not named here for the pleasant time. A special thanks goes to my wife, Sille, who made my time away from work a joy.

I acknowledge financial support from the Information Technology Foundation for Education (HITSA) and Skype Technologies OÜ during my master's studies.

A PycQED measurement and analysis software

In the course of this Master's thesis we used the PycQED software package as the first team in the Quantum Device Lab. PycQED is a Python library initially developed in the DiCarlo group of the Delft University of Technology. This appendix serves the purpose of giving an overview of the library and its concepts for someone who wants to start using it. The main goal of the library is to provide a framework and ready-to-use tools for controlling the experiment's hardware and analyse the measurement results in the context of circuit QED. The latest version of PycQED, which is under constant development, is available in the git repository published on GitHub[1] under the MIT licence. For development of the library in the Quantum Device Lab, we have created a fork of the repository under the QudevETH organization[2].

A.1 Overview of the library

Instruments. For each hardware instrument there is a subclass of the base `Instrument`[3] class that handles communication with the instrument via its member functions and *parameters*. The parameters are instances of the `Parameter`[4] class and are wrappers for normal variables that allow for custom setters and getters that can handle the hardware communication. The driver classes for most instruments that we used and the parameter classes are defined in the QCoDeS[5] library, which PycQED depends upon. Some instruments, like the `Heterodyne`[6] instrument and the qubit classes, do not correspond to any specific hardware, but coordinate the functions of other instruments, and are called meta-instruments. The qubit classes are meta-instruments, that contain references to the instruments relevant for doing single qubit experiments; parameters for single-qubit operation, like qubit frequency and drive pulse parameters; and methods that run the standard qubit characterization measurements. The qubit class that we developed for the experimental setup used in this thesis is the `QuDev_transmon`[7]. For more detailed description of

[1] `https://github.com/DiCarloLab-Delft/PycQED_py3`
[2] `https://github.com/QudevETH/PycQED_py3`
[3] in `qcodes/instrument/base.py`
[4] in `qcodes/instrument/parameter.py`
[5] `https://github.com/QCoDeS/Qcodes`
[6] in `pycqed/instrument_drivers/meta_instrument/heterodyne.py`
[7] in `pycqed/instrument_drivers/meta_instrument/qubit_objects/QuDev_transmon.py`

specific methods and parameters in the `QuDev_transmon`, see Stefania Balasiu's semester thesis [48, sec. 3.2.1].

Measurement control. The central component to running measurements with PycQED is the `MeasurementControl`[1] class. An instance of `MeasurementControl` is set up with a *sweep function*, which is an instance of a class derived from the base `Sweep_function`[2] class and is responsible for setting the parameter values that are varied in the measurement; a list of *sweep points*, which are the values that will be passed to the sweep function; and a *detector function*, which is an instance of a class derived from the base `Detector_Function`[3] class and is responsible for acquiring the data. There are two types of sweep and detector functions, software and hardware controlled, and their type needs to match in a single experiment. In a software controlled sweep the Python program acquires the data using the detector function after each setting of the sweep parameter, while in a hardware controlled sweep all the sweep points are programmed to the hardware at the start of the experiment and extracted with the detector function after the measurement is finished. There is also the option to use a second software sweep function to vary two variables simultaneously in a 2D-sweep. As a special case of the software controlled sweep, adaptive sweeps, where the next sweep points are calculated from the previous measurement results, are also supported. Adaptive sweeps were not used in the course of this thesis, but could be used for example for Nelder-Mead optimization. After finishing the measurement, the results together with the values of all the parameters are automatically saved in the HDF5[4] data format. The `MeasurementControl` can also plot the measurement results as the data is acquired.

Sweep and detector functions. As the most simple case of the software controlled sweep, any instrument parameter can be specified as a sweep function. This is used for example in Listing 2, where the MWG frequency is swept in a transmission spectrum measurement. Another example of a software controlled sweep is the `None_Sweep`[2], which is useful as the second sweep function in a 2D sweep for repeating the first sweep. The hardware controlled sweep functions used in this thesis program the AWG with the waveforms for the subexperiments that are swept over. For this, every experiment has its own AWG *sequence function* that actually creates the pulse sequences and

[1] in `pycqed/measurement/measurement_control.py`
[2] in `pycqed/measurement/sweep_functions.py`
[3] in `pycqed/measurement/detector_functions.py`
[4] `https://support.hdfgroup.org/HDF5/`

programs the AWG, reducing the sweep function to a wrapper that defines the units of the sweep points and implements the interface expected by the `MeasurementControl`. The only software controlled detector function used was the `Heterodyne_probe`[1], which is a wrapper around the data acquisition code in the `Heterodyne` and `LO_modulated_Heterodyne`[2] meta-instruments. It has an unintuitive interface, where some parameters that are defined in the heterodyne classes need to be passed also to the detector function on initialization. The hardware controlled detector functions that we used are `UHFQC_input_average_detector`[1], `UHFQC_integrated_average_detector`[1] and `UHFQC_integration_logging_det`[1]. The input average detector function corresponds to the input average output node in Fig. 8. The sweep points are the samples of timetrace and therefore it does not make sense to use any other sweep function than the `None_Sweep` in this case. The integrated average detector and the integration logging detector correspond to the result logger output node in Fig. 8 and can be configured to output the result from any of the signal processing stages. The difference between the two detectors is that unlike the integrated average detector, the integration logging detector is hard-coded with no averaging and is thereby meant for logging single-shot readout results.

Waveform generation. Programming the AWGs with the desired waveforms is handled by the `Pulsar`[3] class in PycQED. During initialization, the physical AWG channels used are defined in the `Pulsar` with a name that is used to refer to the channel in other parts of the code. When programming the AWGs, the `Pulsar` receives a list of `Element`s,[4] which correspond to the segments that will be programmed to the AWGs and a `Sequence`[5] object that specifies the order and number of repetitions of each segment and whether the playback should wait for a trigger of the AWG. The waveforms are not saved in the `Element`s, but are generated on demand by the `Pulse`[6] objects in the `Element`. The `Pulse` classes get as inputs the time-values and output the waveforms corresponding to these time-values, with the type of the pulse defined by the specific subclass of the base `Pulse` class. When adding pulses to the `Element`, either the absolute starting time or the starting time relative to some other pulse can be specified. For most pulse sequences

[1] in `pycqed/measurement/detector_functions.py`
[2] in `pycqed/instrument_drivers/meta_instrument/heterodyne.py`
[3] in `pycqed/measurement/waveform_control/pulsar.py`
[4] in `pycqed/measurement/waveform_control/element.py`
[5] in `pycqed/measurement/waveform_control/sequence.py`
[6] in `pycqed/measurement/waveform_control/pulse.py`

the `multi_pulse_elt`[1] function, that generates an `Element` from a list of *pulse dictionaries*, is used. A pulse dictionary is a Python dictionary that contains the pulse type, its parameters and its start time relative to the previous added pulse. For single qubit gates, the pulse dictionaries are compiled from the parameters in the qubit object by qubit methods.

Measurement Analysis. A useful feature of PycQED is that the analysis for standard experiments is included in the same library as the measurement code. This enables quick reuse of the results from previous experiments. For each experiment type there is an analysis class that derives from the base `MeasurementAnalysis`[2]. The experimental data is loaded from the HDF5 file generated by the `MeasurementControl` and the results are saved in the same file. For a more detailed description of how the analysis classes work, see Stefania Balasiu's semester thesis [48, sec. 3.2.3].

A.2 Added functionality

To be able to use the PycQED library for multiplexed readout with the hardware setup in our lab, several missing features had to be implemented. First, the initial version of the `QuDev_transmon` was created, as each qubit object in PycQED relies on specific hardware, and ours differs from what existed in PycQED.

In addition the drivers for the Stanford Research Systems SIM928 isolated voltage source module and the Advantech PCIE-1751 digital input-output card were created, which we use for dc-biasing the fluxlines and the coils and for switching the microwave switches for bypassing the upconversion mixer of the drive pulses (see section 3.2) respectively. These drivers we contributed to the QCoDeS library as they are useful for a wider audience. A meta-instrument `ConversionBoxControl`[3] specific to the microwave-switches in our setup was also created that uses the more general PCIE-1751 hardware driver.

Because of the relatively large number of qubits on our sample, we needed to use two Tektronix AWG5014 instruments to generate the drive pulses. For this the `Pulsar` class was updated with

[1] in `pycqed/measurement/pulse_sequences/standard_elements.py`
[2] in `pycqed/analysis/measurement_analysis.py`
[3] in the PycQED_Scripts Subversion repository `pycqedscripts/drivers/conversion_box_control.py`

support for multiple AWGs. The update also added rudimentary support for using the UHFQC as an AWG in the same framework.

Last, the pulse sequences for the multiplexed readout experiment the cross-dephasing measurement were created.

A.3 Useful code snippets

In this section a series of example code-snippets for the basic tasks with PycQED are presented.

Listing 1: Initialization of the instruments used for spectroscopy. Each instrument is added to the `Station`[1] object using the `station.add_component` method to make its parameters available to the `MeasurementControl` object for automatic saving.

```
import numpy as np
import pycqed
import pycqed.measurement.detector_functions as det
import pycqed.analysis.measurement_analysis as ma
import qcodes
from qcodes.instrument_drivers.rohde_schwarz import SGS100A
from qcodes.instrument_drivers.stanford_research import SIM928
from qcodes.instrument_drivers.tektronix import AWG5014
from pycqed.instrument_drivers.meta_instrument import heterodyne
from pycqed.instrument_drivers.physical_instruments.ZurichInstruments import UHFQuantumController
from pycqed.measurement import measurement_control
from pycqed.measurement.pulse_sequences import standard_sequences, single_qubit_tek_seq_elts, multi_qubit_tek_seq_elts
# set the data saving directory
pycqed.analysis.analysis_toolbox.datadir = r'E:\data'
station = qcodes.Station()
# Initialize the R&S SGS100A microwave generator driver
MWG1 = SGS100A.RohdeSchwarz_SGS100A(name='MWG1', address='TCPIP0::192.168.1.35')
station.add_component(MWG1)
MWG1.power(25)
# Initialize the Tektronix AWG5014 instrument driver
AWG = AWG5014.Tektronix_AWG5014(name='AWG', address='TCPIP0::192.168.1.4')
station.add_component(AWG)
AWG.set_current_folder_name(r"C:\temp\PycQEDwaveforms")
AWG.write('SOUR1:ROSC:SOUR EXT') # Use external reference clock
# Initialize the ZI UHFQC instrument driver
UHFQC = UHFQuantumController.UHFQC(name='UHFQC', device='dev2204', port=8004)
station.add_component(UHFQC)
UHFQC.triggers_in_0_level(0.5)
# Initialize the SRS SIM928 battery instrument driver. The battery that is connected to the coil is in module 1.
DC_source = SIM928.SIM928(name='DC_source', address='GPIB0::30::INSTR', slot_names={1: 'coil_5'})
station.add_component(DC_source)
```

[1] in `qcodes/station.py`

```
# Create the homodyne metainstrument for spectroscopy measurements
homodyne = heterodyne.LO_modulated_Heterodyne(name='homodyne', LO=MWG1, AWG=AWG, acquisition_instr='UHFQC')
homodyne.acq_marker_channels('AWG_ch3_marker2')
# Initialize the measurement control object
MC = pycqed.measurement.measurement_control.MeasurementControl(name='MC')
station.add_component(MC)
MC.station = station
# Initialize the pulsar.
pulsar = pycqed.measurement.waveform_control.pulsar.Pulsar(master_AWG=AWG.name)
station.add_component(pulsar)
# The pulsar is added to the station object and the station is added to the pulse sequence modules so that the pulse
# sequence modules have a reference to the pulsar and can upload the waveforms to the hardware.
station.pulsar = pulsar
standard_sequences.station = station
single_qubit_tek_seq_elts.station = station
multi_qubit_tek_seq_elts.station = station
# The AWG channels need to be registered with the pulsar
for i in range(1, 5):
    pulsar.define_channel(id='ch{}'.format(i), type='analog', name='{}_ch{}'.format(AWG.name, i), high=2, low=-2,
                          offset=0, delay=0, active=True, AWG=AWG.name)
    pulsar.define_channel(id='ch{}_marker1'.format(i), name='{}_ch{}_marker1'.format(AWG.name, i), type='marker',
                          high=2.7, low=0, offset=0, delay=0, active=True, AWG=AWG.name)
    pulsar.define_channel(id='ch{}_marker2'.format(i), name='{}_ch{}_marker2'.format(AWG.name, i), type='marker',
                          high=2.7, low=0, offset=0, delay=0, active=True, AWG=AWG.name)
pulsar.channels['AWG_ch3_marker2']['high'] = 1 # Set UHFQC trigger amp.
```

Listing 2: An example of a 1D software sweep: a resonator spectroscopy measurement.

```
homodyne.RO_length(2.275e-6)         # Set the readout pulse length to the maximal supported value.
homodyne.trigger_separation(3e-6)    # Set the repetition rate of the experiment
homodyne.mod_amp(0.05)               # Set the amplitude of the readout pulse
homodyne.nr_averages(2**8)           # Do 256 averages
homodyne.f_RO_mod(450e6)             # Set the readout modulation frequency
homodyne.single_sideband_demod(True) # Use the signal in both input channels of the UHFQC
MC.set_sweep_function(homodyne.frequency)
MC.set_sweep_points(np.linspace(6.2e9, 7.2e9, 1001))
MC.set_detector_function(det.Heterodyne_probe(homodyne, trigger_separation=homodyne.trigger_separation(),
    demod_mode='single' if homodyne.single_sideband_demod() else 'double', RO_length=homodyne.RO_length()))
MC.run(name='resonator_scan_homodyne')
ma.MeasurementAnalysis()             # Create a plot of the measurement results
```

Listing 3: An example of a 2D software sweep: a resonator spectroscopy – coil voltage measurement.

```
MC.set_sweep_function(homodyne.frequency)
MC.set_sweep_points(np.linspace(6.2e9, 7.2e9, 1001))
MC.set_sweep_function_2D(DC_source.volt_coil_5)
MC.set_sweep_points_2D(np.linspace(-0.3, 0.3, 21))
MC.set_detector_function(det.Heterodyne_probe(homodyne, trigger_separation=homodyne.trigger_separation(),
    demod_mode='single' if homodyne.single_sideband_demod() else 'double', RO_length=homodyne.RO_length()))
MC.run(name='resonator_flux_scan_homodyne', mode='2D')
ma.MeasurementAnalysis(TwoD=True)
```

Listing 4: A QuDev_transmon qubit object is initialized and its parameters are set.

```
from qcodes.instrument_drivers.Advantech import PCIE_1751
from pycqed.instrument_drivers.meta_instrument import conversion_box_control
from pycqed.instrument_drivers.meta_instrument.qubit_objects import QuDev_transmon
MWG2 = SGS100A.RohdeSchwarz_SGS100A(name='MWG2', address='TCPIP0::192.168.1.36')
station.add_component(MWG2)
# Initialize the mixer bypass switch control instruments
DIO = PCIE_1751.Advantech_PCIE_1751('DIO')
station.add_component(DIO)
SwitchControl = conversion_box_control.ConversionBoxControl(name='SwitchControl', dio=DIO)
station.add_component(SwitchControl)
SwitchControl.set_switch({'UC2': 'modulated'})
# Create the qubit meta-instrument
qb = QuDev_transmon.QuDev_transmon(name='qb', MC=MC, heterodyne=homodyne, cw_source=MWG2, readout_DC_LO=MWG1,
        readout_UC_LO=MWG1, drive_LO=MWG2, AWG=pulsar, UHFQC=UHFQC)
station.add_component(qb)
# Readout parameters
qb.RO_pulse_type('MW_IQmod_pulse_UHFQC')
qb.RO_acq_marker_channel('AWG_ch3_marker2');              qb.RO_pulse_marker_channel('AWG_ch3_marker2')
qb.RO_acq_weight_function_I(0);                           qb.RO_acq_weight_function_Q(1)
qb.RO_I_channel('0');                                     qb.RO_Q_channel('1')
qb.f_RO(7.0601e9);                                        qb.f_RO_mod(450e6)
qb.RO_acq_averages(2**10);                                qb.RO_amp(0.05)
qb.RO_pulse_length(2.2e-6);                               qb.RO_acq_integration_length(2.2e-6)
qb.RO_acq_marker_delay(-176e-9);                          qb.RO_pulse_delay(0)
qb.set_default_readout_weights()
# Drive pulse parameters
qb.pulse_type('SSB_DRAG_pulse')
qb.pulse_I_channel('AWG_ch1');                            qb.pulse_Q_channel('AWG_ch2')
qb.f_qubit(6.17642e9);                                    qb.f_pulse_mod(100e6)
qb.X_pulse_phase(0);                                      qb.X_pulse_phase_ef(0)
qb.pulse_delay(0);                                        qb.motzoi(0)
qb.gauss_sigma(10e-9);                                    qb.nr_sigma(5)
qb.phi_skew(0);                                           qb.alpha(1)
qb.drive_LO_pow(22)
```

Listing 5: Rabi, Ramsey and single shot readout fidelity experiments are conducted sequentially. 1D hardware sweeps are used in the QuDev_transmon.measure_rabi and QuDev_transmon.measure_ramsey methods, which are called by the find_amplitudes and find_frequency_T2_ramsey methods here. The QuDev_transmon.find_ssro_fidelity method uses a 2D sweep where an inner hardware controlled sweep using the integrated logging detector is repeated using an outer None_Sweep.

```
qb.find_amplitudes(rabi_amps=np.linspace(0, 0.5, 61), update=True)
qb.find_frequency_T2_ramsey(np.linspace(0, 2e-6, 101), artificial_detuning=5e6, update=True)
qb.find_ssro_fidelity(nreps=50)
```

References

[1] Heebyung Koh and Christopher L. Magee. A functional approach for studying technological progress: Application to information technology. *Technological Forecasting and Social Change*, 73(9):1061 – 1083, 2006.

[2] Richard P. Feynman. Simulating physics with computers. *Int. J. Theor. Phys.*, 21(6):467–488, June 1982.

[3] P. W. Shor. Algorithms for quantum computation: Discrete logarithms and factoring. In *Proceedings, 35th Annual Symposium on Foundations of Computer Science, Santa Fe*, page 124. IEEE Computer Society Press, 1994.

[4] Lov K. Grover. A fast quantum mechanical algorithm for database search. In *Proceedings of the twenty-eighth annual ACM symposium on Theory of computing*, pages 212–219, Philadelphia, Pennsylvania, United States, 1996. ACM.

[5] Patrick Rebentrost, Masoud Mohseni, and Seth Lloyd. Quantum support vector machine for big data classification. *Phys. Rev. Lett.*, 113:130503, Sep 2014.

[6] Aram W. Harrow, Avinatan Hassidim, and Seth Lloyd. Quantum algorithm for linear systems of equations. *Phys. Rev. Lett.*, 103:150502, Oct 2009.

[7] M. Brune, F. Schmidt-Kaler, A. Maali, J. Dreyer, E. Hagley, J. M. Raimond, and S. Haroche. Quantum Rabi oscillation: A direct test of field quantization in a cavity. *Phys. Rev. Lett.*, 76(11):1800–1803, Mar 1996.

[8] C. Monroe, D. M. Meekhof, B. E. King, W. M. Itano, and D. J. Wineland. Demonstration of a fundamental quantum logic gate. *Phys. Rev. Lett.*, 75:4714–4717, Dec 1995.

[9] David G. Cory, Amr F. Fahmy, and Timothy F. Havel. Ensemble quantum computing by NMR spectroscopy. *Proceedings of the National Academy of Sciences*, 94(5):1634–1639, March 1997.

[10] F. Yamaguchi and Y. Yamamoto. Crystal lattice quantum computer. *Applied Physics A*, 68(1):1–8, Jan 1999.

[11] Daniel Loss and David P. DiVincenzo. Quantum computation with quantum dots. *Phys. Rev. A*, 57(1):120–, January 1998.

[12] E. Knill, R. Laflamme, and G. J. Milburn. A scheme for efficient quantum computation with linear optics. *Nature*, 409(6816):46–52, January 2001.

[13] F. Jelezko, T. Gaebel, I. Popa, A. Gruber, and J. Wrachtrup. Observation of coherent oscillations in a single electron spin. *Phys. Rev. Lett.*, 92:076401, Feb 2004.

[14] Alexandre Blais, Ren-Shou Huang, Andreas Wallraff, S. M. Girvin, and R. J. Schoelkopf. Cavity quantum electrodynamics for superconducting electrical circuits: An architecture for quantum computation. *Phys. Rev. A*, 69:062320, Jun 2004.

[15] D. Gottesman. *Stabilizer Codes and Quantum Error Correction.* PhD thesis, California Institute of Technology, 1997.

[16] R. Versluis, S. Poletto, N. Khammassi, N. Haider, D. J. Michalak, A. Bruno, K. Bertels, and L. DiCarlo. Scalable quantum circuit and control for a superconducting surface code. *arXiv:1612.08208*, 2016.

[17] Austin G. Fowler, Matteo Mariantoni, John M. Martinis, and Andrew N. Cleland. Surface codes: Towards practical large-scale quantum computation. *Phys. Rev. A*, 86:032324, Sep 2012.

[18] Michael A. Nielsen and Isaac L. Chuang. *Quantum Computation and Quantum Information.* Cambridge University Press, 2010.

[19] E.T. Jaynes and F.W. Cummings. Comparison of quantum and semiclassical radiation theories with application to the beam maser. *Proceedings of the IEEE*, 51(1):89–109, 1963.

[20] A. Wallraff, D. I. Schuster, A. Blais, L. Frunzio, R.-S. Huang, J. Majer, S. Kumar, S. M. Girvin, and R. J. Schoelkopf. Strong coupling of a single photon to a superconducting qubit using circuit quantum electrodynamics. *Nature*, 431:162–167, 2004.

[21] Y. Nakamura, Y. A. Pashkin, and J. S. Tsai. Coherent control of macroscopic quantum states in a single-Cooper-pair box. *Nature*, 398(6730):786–788, April 1999.

[22] Jens Koch, Terri M. Yu, Jay Gambetta, A. A. Houck, D. I. Schuster, J. Majer, Alexandre Blais, M. H. Devoret, S. M. Girvin, and R. J. Schoelkopf. Charge-insensitive qubit design derived from the Cooper pair box. *Phys. Rev. A*, 76(4):042319, 2007.

[23] V. B. Braginsky and F. Ya. Khalili. Quantum nondemolition measurements: the route from toys to tools. *Rev. Mod. Phys.*, 68:1–11, Jan 1996.

[24] D. I. Schuster, A. Wallraff, A. Blais, L. Frunzio, R.-S. Huang, J. Majer, S. M. Girvin, and R. J. Schoelkopf. AC Stark shift and dephasing of a superconducting qubit strongly coupled to a cavity field. *Phys. Rev. Lett.*, 94(12):123602, April 2005.

[25] C. W. Gardiner and M. J. Collett. Input and output in damped quantum systems: Quantum stochastic differential equations and the master equation. *Phys. Rev. A*, 31(6):3761–3774, 1985.

[26] D. F. Walls and G. J. Milburn. *Quantum Optics*. Springer Verlag, Berlin, 2 edition, 2008.

[27] C. M. Caves. Quantum limits on noise in linear amplifiers. *Phys. Rev. D*, 26:1817–1839, 1982.

[28] B Peropadre, J Lindkvist, I-C Hoi, C M Wilson, J J Garcia-Ripoll, P Delsing, and G Johansson. Scattering of coherent states on a single artificial atom. *New J. Phys.*, 15(3):035009, 2013.

[29] C. Eichler, D. Bozyigit, and A. Wallraff. Characterizing quantum microwave radiation and its entanglement with superconducting qubits using linear detectors. *Phys. Rev. A*, 86:032106, Sep 2012.

[30] D. M. Pozar. *Microwave engineering*. Wiley & Sons, Hoboken, 2012.

[31] Guanbin Xing, Manyuan Shen, and Hui Liu. Frequency offset and i/q imbalance compensation for direct-conversion receivers. *IEEE Transactions on Wireless Communications*, 4(2):673–680, 2005.

[32] Christopher Eichler and Andreas Wallraff. Controlling the dynamic range of a josephson parametric amplifier. *EPJ Quantum Technology*, 1(1):2, 2014.

[33] C. Macklin, K. O'Brien, D. Hover, M. E. Schwartz, V. Bolkhovsky, X. Zhang, W. D. Oliver, and I. Siddiqi. A near-quantum-limited josephson traveling-wave parametric amplifier. *Science*, 350(6258):307–310, 2015.

[34] T. Walter, P. Kurpiers, S. Gasparinetti, P. Magnard, A. Potocnik, Y. Salathé, M. Pechal, M. Mondal, M. Oppliger, C. Eichler, and A. Wallraff. Rapid, high-fidelity, single-shot dispersive readout of superconducting qubits. *Phys. Rev. Applied*, 7:054020, 2017.

[35] Isaac L. Chuang and M. A. Nielsen. Prescription for experimental determination of the dynamics of a quantum black box. *J. Mod. Opt.*, 44(11):2455–2467, 1997.

[36] Seth T. Merkel, Jay M. Gambetta, John A. Smolin, Stefano Poletto, Antonio D. Córcoles, Blake R. Johnson, Colm A. Ryan, and Matthias Steffen. Self-consistent quantum process tomography. *Phys. Rev. A*, 87:062119, Jun 2013.

[37] C. C. Bultink, B. Tarasinski, N. Haandbaek, S. Poletto, N. Haider, D. J. Michalak, A. Bruno, and L. DiCarlo. General method for extracting the quantum efficiency of dispersive qubit readout in circuit qed. *arXiv:1711.05336*, 2017.

[38] J. Heinsoo, C. K. Andersen, A. Remm, S. Krinner, T. Walter, Y. Salathe, S. Gasperinetti, J.C. Besse, A. Potocnik, C. Eichler, and A. Wallraff. Rapid high-fidelity multiplexed readout of superconducting qubits. *To be published*, 2017.

[39] Lars Steffen. *Quantum Teleportation and Efficient Process Verification with Superconducting Circuits*. PhD thesis, ETH Zurich, 2013.

[40] Johannes Fink. *Quantum nonlinearities in strong coupling circuit QED*. PhD thesis, ETH Zurich, 10 2010.

[41] R. Barends, J. Kelly, A. Megrant, D. Sank, E. Jeffrey, Y. Chen, Y. Yin, B. Chiaro, J. Mutus, C. Neill, P. O'Malley, P. Roushan, J. Wenner, T. C. White, A. N. Cleland, and John M. Martinis. Coherent josephson qubit suitable for scalable quantum integrated circuits. *Phys. Rev. Lett.*, 111(8):080502–, August 2013.

[42] Johannes Heinsoo. Towards high fidelity two-qubit gates with superconducting qubits. Master's thesis, ETH Zurich, 06 2014.

[43] Christian Lang. *Quantum Microwave Radiation and its Interference Characterized by Correlation Function Measurements in Circuit Quantum Electrodynamics*. PhD thesis, ETH Zurich, 02 2014.

[44] A. Wallraff, D. I. Schuster, A. Blais, J. M. Gambetta, J. Schreier, L. Frunzio, M. H. Devoret, S. M. Girvin, and R. J. Schoelkopf. Sideband transitions and two-tone spectroscopy of a superconducting qubit strongly coupled to an on-chip cavity. *Phys. Rev. Lett.*, 99:050501, 2007.

[45] F. Motzoi, J. M. Gambetta, P. Rebentrost, and F. K. Wilhelm. Simple pulses for elimination of leakage in weakly nonlinear qubits. *Phys. Rev. Lett.*, 103(11):110501, 2009.

[46] J. Gambetta, A. Blais, M. Boissonneault, A. A. Houck, D. I. Schuster, and S. M. Girvin. Quantum trajectory approach to circuit QED: Quantum jumps and the zeno effect. *Phys. Rev. A*, 77:012112, 2008.

[47] C. Jones, M. F. Gyure, T. D. Ladd, M. A. Fogarty, A. Morello, and A. S. Dzurak. A logical qubit in a linear array of semiconductor quantum dots. *arXiv:1608.06335*, 2016.

[48] Stefania Balasiu. Single-qubit gates calibration in pycqed using superconducting qubits, 2017. Semester thesis, ETH Zurich.

ETH

Eidgenössische Technische Hochschule Zürich
Swiss Federal Institute of Technology Zurich

Declaration of originality

The signed declaration of originality is a component of every semester paper, Bachelor's thesis, Master's thesis and any other degree paper undertaken during the course of studies, including the respective electronic versions.

Lecturers may also require a declaration of originality for other written papers compiled for their courses.

I hereby confirm that I am the sole author of the written work here enclosed and that I have compiled it in my own words. Parts excepted are corrections of form and content by the supervisor.

Title of work (in block letters):

IMPLEMENTATION AND CHARACTERIZATION OF MULTIPLEXED READOUT OF SUPERCONDUCTING QUBITS

Authored by (in block letters):

For papers written by groups the names of all authors are required.

Name(s):	**First name(s):**
REMM	ANTS

With my signature I confirm that

- I have committed none of the forms of plagiarism described in the 'Citation etiquette' information sheet.
- I have documented all methods, data and processes truthfully.
- I have not manipulated any data.
- I have mentioned all persons who were significant facilitators of the work.

I am aware that the work may be screened electronically for plagiarism.

Place, date	**Signature(s)**
Zurich, 20.11.2017	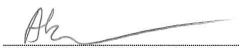

For papers written by groups the names of all authors are required. Their signatures collectively guarantee the entire content of the written paper.